



HAL
open science

Intraplate orogenesis as a driver of multistage karst-hosted mineralization: the Imini manganese case (Atlas, Morocco)

Augustin Dekoninck, Jocelyn Barbarand, Gilles Ruffet, Yves Missenard, Nadine Mattielli, Rémi Leprêtre, Abdellah Mouttaqi, Michèle Verhaert, Omar Saddiqi, Johan Yans

► To cite this version:

Augustin Dekoninck, Jocelyn Barbarand, Gilles Ruffet, Yves Missenard, Nadine Mattielli, et al.. Intraplate orogenesis as a driver of multistage karst-hosted mineralization: the Imini manganese case (Atlas, Morocco). *Mineralium Deposita*, 2024, 59 (3), pp.453-472. 10.1007/s00126-023-01212-9 . insu-04230605

HAL Id: insu-04230605

<https://insu.hal.science/insu-04230605>

Submitted on 6 Oct 2023

HAL is a multi-disciplinary open access archive for the deposit and dissemination of scientific research documents, whether they are published or not. The documents may come from teaching and research institutions in France or abroad, or from public or private research centers.

L'archive ouverte pluridisciplinaire **HAL**, est destinée au dépôt et à la diffusion de documents scientifiques de niveau recherche, publiés ou non, émanant des établissements d'enseignement et de recherche français ou étrangers, des laboratoires publics ou privés.

1 **Intraplate orogenesis as a driver of multistage karst-hosted mineralization: the Imini manganese case**
2 **(Atlas, Morocco)**

3 Augustin DEKONINCK^{(1,2)@}, Jocelyn BARBARAND⁽³⁾, Gilles RUFFET^(4,5), Yves MISSENARD⁽³⁾, Nadine
4 MATTIELLI⁽²⁾, Rémi LEPRETRE^(3,6), Abdellah MOUTTAQI⁽⁷⁾, Michèle VERHAERT⁽¹⁾, Omar SADDIQI⁽⁸⁾,
5 Johan YANS⁽¹⁾

6 (1) Département de géologie, Institute of Life, Earth and Environment (ILEE), Université de Namur, 61 rue
7 de Bruxelles, 5000 Namur, Belgium ; augustin.dekoninck@unamur.be (corresponding author)

8 johan.yans@unamur.be, michele.verhaert@hotmail.com

9 (2) Laboratoire G-Time, Department of Geosciences, Environment and Society (DGES) Université Libre de
10 Bruxelles (ULB), 50 (CP 160/02), Av. FD Roosevelt, 1050 Brussels, Belgium; nadine.mattielli@ulb.be,

11 augustin.dekoninck@ulb.be

12 (3) UMR GEOPS, Université Paris Saclay, CNRS, rue du Belvédère, 91405 Orsay Cedex, France;

13 yves.missenard@universite-paris-saclay.fr, jocelyn.barbarand@universite-paris-saclay.fr

14 (4) CNRS (CNRS/INSU), UMR 6118 Géosciences Rennes, 35042 Rennes Cedex, France;

15 gilles.ruffet@univ-rennes1.fr

16 (5) Université de Rennes, Géosciences Rennes, 35042 Rennes Cedex, France; gilles.ruffet@univ-rennes1.fr

17 (6) CY Cergy Paris Université, Géosciences et Environnement Cergy (GEC), 1 rue Descartes, 95000

18 Neuville-s-Oise Cedex, France. remi.lepretre@cyu.fr

19 (7) Office National des Mines et des Hydrocarbures (ONHYM), 5 Charia My Hassan, BP99, Rabat,

20 Morocco ; mouttaqi@onhym.com

21 (8) Laboratoire Géosciences, Université Hassan II, BP 5366, Maârif, 20100 Casablanca, Morocco ;

22 omarsaddiqi@yahoo.fr

23 Corresponding author: Augustin Dekoninck – augustin.dekoninck@unamur.be

24

25 **Abstract**

26 The Imini mining district (southern foreland of the intraplate Atlasic belt of Morocco) hosts the largest Mn
27 resources of North Africa, consisting of two laterally extensive bodies of high-grade pyrolusite-rich manganese
28 ore and a third discontinuous medium-grade coronadite-rich Mn ore hosted in a ~10-15 meters thick Cenomanian-
29 Turonian dolostone unit. Until now, the origin and timing of the Mn ore have been poorly constrained. New Pb
30 isotopic ratios show that Triassic series (basalts and red sandstone) are likely the source of the metals. $^{40}\text{Ar}/^{39}\text{Ar}$
31 dating of K-Mn oxides shows that the Mn-rich orebodies formed during at least three periods: late Cretaceous to
32 late Paleocene (>58 Ma), late Eocene (ca. 36.3 Ma), and early Burdigalian to early Serravalian probably in two
33 pulses at ca. 19–20 Ma and ca. 13 Ma. These periods coincide with three known building phases of the Atlasic
34 relief during late Cretaceous, late Eocene and the Early(?)–Middle Miocene. We therefore propose the Atlasic
35 tectonics as the first-order control of the Mn mineralization. Periods with regionally high elevations modified the
36 climate to wetter conditions that supplied meteoric water to feed temporary aquifers. Relief building created the
37 required hydraulic head to sustain (1) fluid-rock interaction between O_2 -poor acidic fluids and the Triassic series,
38 (2) migration of the metal-rich fluid and (3) to overpressure fluid in the Imini depositional site. The decreasing
39 thickness of Triassic series in front of the Imini anticline forced these low-temperature (<100°C) fluids to mix
40 with oxygenated and alkaline ground waters in the karst system and precipitate Mn oxides. The N70°-oriented
41 Atlasic tectonic structure controls the orientation of the Mn deposits. The late Eocene – Early/Middle Miocene
42 uplifts generated additional supplies and/or in-situ remobilization of the primary late Cretaceous medium-grade
43 ore to form the high-grade pyrolusite-rich ore.

44 **Keywords:** $^{39}\text{Ar}/^{40}\text{Ar}$ dating, Pb isotopes, geodynamics, ore deposits, K-Mn oxides

45

46 **Introduction**

47 Understanding the genesis and evolution of an ore requires different components of the metallogenic system:
48 fertility of the source(s), transport and concentration of metals including mineralizing fluid movement,
49 geodynamic setting and triggering events, accumulation and preservation of the metals (e.g., Laznicka 2014;
50 McCuaig et al. 2018). The geodynamic phases that affect the distribution of rocks and the building of relief may
51 modify, distance, or remove the source rocks. These changes can also determine the preferential paths followed
52 by the mineralizing fluids and consequently control the timing and duration of metal deposition (e.g. Groves and
53 Bierlein, 2007). The timing and identification of metal sources are required to describe and characterize the
54 mineral system and its connection to geological settings.

55 The karst-hosted Imini manganese district is a good example to investigate the geodynamic control of the
56 mineralization process as (i) it is located in the vicinity of the intraplate Atlas orogenic belt of Morocco (Frizon
57 de Lamotte et al. 2000) (Figs. 1 and 2), where the tectonic history is relatively well-constrained (Leprêtre et al.
58 2015), (ii) K-bearing Mn oxides in the ore can be dated and (iii) several potential source rocks are available
59 (Gutzmer et al. 2006; Dekoninck et al. 2016b, a, 2021). Several models have been proposed to explain the high-
60 grade Mn ore hosted in the ~10-15 m-thick Cenomanian-Turonian (CT) dolostone involving sedimentary-
61 diagenetic and hydrothermal models (Dekoninck et al. 2016b). According to Gutzmer et al. (2006) and Dekoninck
62 et al. (2016a, 2021), the Mn mineralization process involved multistage karst-related epigenesis by mixing of low-
63 temperature groundwater and oxidizing meteoric water. The Imini district has the highest economic Mn grades of
64 North Africa due to the presence of two pyrolusite-rich stratabound ore (C1 and C2), and a third horizon (C3)
65 predominantly composed of coronadite group minerals (Beaudoin et al. 1976). The C1 and C2 ore occur over a
66 ~25–30 km strike length forming the Imini district (Fig. 2a), whereas the C3 ore occurs discontinuously over
67 ~100 km from Imini to Tasdremt (Dekoninck et al. 2021)(Fig. 1). The timing of the Imini mineralization has not
68 been investigated so far despite the presence of K-Mn oxides. In the Tasdremt area (Fig. 1b), Dekoninck et al.
69 (2021) have shown that the Mn ore is similar to the C3 ore at Imini and formed during three mineralizing periods
70 at ~91.5 Ma, ~77.5–82 Ma, and ~65–67 Ma. Likewise, source rocks of the Mn mineralization have remained
71 speculative (Gutzmer et al. 2006; Dekoninck et al. 2016b, 2021). The possible sources include : (i) the voluminous
72 Neoproterozoic volcanic basement hosting numerous Mn-rich veins in the Anti-Atlas (Choubert and Faure-Muret,
73 1973) or (iii) the large Triassic basaltic rocks of the Central Atlantic Magmatic Province and red sandstone in the
74 Atlas (CAMP; Marzoli et al., 2019).

75 The aim of this study is to propose an integrated model of the karst-hosted Imini manganese deposits, from
76 the source to ore deposition, in light of a structural study in the Imini area (Leprêtre et al. 2015) and detailed
77 petrographic/mineralogical investigations of the manganiferous orebodies (Dekoninck et al. 2016a, 2021), with
78 new Pb isotope constraints and $^{40}\text{Ar}/^{39}\text{Ar}$ dating of K-bearing coronadite group minerals.

79 **1. Geological setting**

80 **1.1. Regional geology**

81 The Imini Mn district is located at the junction of the High Atlas and the Anti-Atlas (Figs. 1 and 2a), along
82 the western end of the Cenozoic Ouarzazate foreland basin filled by Cenozoic syn- and post tectonic rocks (Figs.
83 1 and 2a). To the north, the area consists of thick Triassic series with basaltic rocks and Fe-rich sandstone overlain
84 by Jurassic carbonates, Cenomanian red sandstones, Cenomanian-Turonian (CT) carbonates (~10-15 m; Fig. 2b),
85 Senonian series (~160 m), of interbedded marls, evaporites and dolostones (Algouti et al., 1999; Rhalmi, 1992),
86 Eocene and Miocene continental to shallow marine rocks as well as Plio-Quaternary alluvium (El Harfi et al.
87 2001) (Figs. 2a and c). The cumulated thickness of the late Cretaceous to Pliocene sediments does not exceed 380
88 meters in the Imini area. Triassic red sandstone and basaltic rocks, together with Liassic limestones thin to the
89 south (Fig. 2c). They pinch out against Neoproterozoic or Ordovician rocks along the Imini anticline, with a N90°
90 strike becoming ENE–WSW east of the Imini anticline (Fig. 2c; Missenard et al. 2007; Leprêtre et al. 2015). The
91 CT carbonates overlie either conformably the poorly dated Lower Cretaceous red sandstones or unconformably
92 the Neoproterozoic volcanic rocks of the Anti-Atlas (Ouarzazate Group) (Thomas et al. 2004) or Ordovician shales
93 (Figs. 2a and c). The CT carbonate succession does not exceed 10-15 m in thickness and has a strong terrigenous
94 component (Fig. 2b; Rhalmi et al., 1997). Senonian formations consist of more than 100 m of red to pink
95 argillaceous sandstones, clays and evaporites (Fig. 2a) likely of Upper Santonian age (Algouti et al., 1999). These
96 rocks are covered by >100 m-thick marine and siliciclastic Eocene carbonate, and Miocene lacustrine carbonate
97 and conglomerate (El Harfi et al. 2001).

98 **1.2. Geodynamic evolution**

99 Early late Cretaceous deformation was documented in several studies (Martin 1982; Froitzheim 1984; Froitzheim
100 et al. 1988; Herbig 1988; Algouti et al. 1999; Fekkak et al. 2018; Cavallina et al. 2018). After an onset of
101 deformation during the late Cretaceous, three tectonic pulses are reported in the High Atlas (Leprêtre et al. 2015,
102 2018). These events are in broad agreement with tectonic events along the whole Atlas belt and elsewhere in the
103 other domains of Morocco (Frizon de Lamotte *et al.*, 2000, 2009). A late Eocene event resulted in large folds with

104 low amplitude along a ~N70° direction. An early to middle Miocene uplift induced cover deformation resulting
105 in gravity sheets and “décollement” nappes, recorded in the Marrakech High Atlas, only. Finally, the Plio-
106 Quaternary shortening reactivated basement faults (Figs. 2a and c). These inherited ~N70° striking faults were
107 possibly also active during the Miocene (Leprêtre et al. 2015; Lanari et al. 2020).

108 Three main deformation styles are recognized in the Atlas of Morocco (Frizon de Lamotte et al. 2000, 2008,
109 2009; Leprêtre et al. 2015). First, the late Cretaceous tectonic regime was responsible for low stand reliefs in
110 association with lithospheric buckling, under the compressional regime due to Africa-Europe convergence (Frizon
111 de Lamotte et al. 2009; Leprêtre et al. 2018). Second, the Late Eocene and Plio-Quaternary accounted for
112 orographic relief when compressional tectonic led to significant faulting and folding,. Third, the Miocene style
113 was, in part, due to thermal uplift, which might be controlled by a lithospheric anomaly (Missenard et al. 2006;
114 Fullea et al. 2010; Lanari et al. 2020, 2022). The late Cretaceous and Miocene phases are thought to have led to
115 minimal deformation of the foreland basins (Fig. 1) and are likely associated with limited erosion.

116 The main regional tectonic structure of the Imini area is an E-W anticline – the Imini fold (Figs. 2a and c).
117 The rocks and Mn orebodies around this structure are cut by faults and flexures (Missenard et al. 2007). The
118 southern limb of the Imini anticline shows higher deformation with local vertical bedding including the CT
119 dolostone and associated Mn orebodies (Figs. 3a-b; Timkit site; Leprêtre *et al.* 2015). Manganese deposits are
120 folded on the northern limb of the anticline (Figs. 2a, 3b). Post-Senonian deformation is marked by steep drag
121 folding of the manganese-bearing carbonate unit and the overlying Senonian red beds. Cenozoic shortening led to
122 tectonic inversion of these structures and numerous N70° small-scale flexures of metric to decametric amplitude
123 (Fig. 3c). In the Lantenois mining site (Fig. 2a), a flexure of the CT dolostone marks the boundary between
124 mineralized and barren zones (Fig. 3c). These structures fold the CT, Senonian and Eocene cover and display
125 symmetric cylinder shape (Figs. 2a).

126 **1.3. Manganese ore style and paragenesis**

127 The manganese ores are hosted in a 10–15 m thick Cenomanian-Turonian (CT) dolostone unit (Thein 1990;
128 Dekoninck et al. 2021, Fig. 1b). In the Imini area, the manganese karst-hosted orebodies are aligned along an
129 ENE-WSW strike forming a narrow horizon (25–30 km in length with a thickness of 400-1000 m; Figs. 2a and
130 3). Mining activity is mostly concentrated on the C1 and C2 levels (Figs 3a-d), which have the highest Mn grades
131 (74-92% MnO₂) due to the massive late stage pyrolusite (Fig. 4). The uppermost C3 level (Figs. 3a, d and e) is
132 predominantly composed of coronadite group minerals [(K,Ba,Pb)Mn₈O₁₆: cryptomelane, hollandite and

133 coronadite] that provide a metallurgic ore (40–48% Mn; Gutzmer et al. 2006; Rhalmi et al. 2011; Dekoninck et
134 al. 2016b). Extensive stockwork mineralization occurs between the Mn orebodies (Gutzmer et al. 2006). Both
135 pyrolusite and coronadite group minerals occur in the three orebodies and in fractures (Gutzmer et al. 2006;
136 Dekoninck et al. 2016a). In the early stage, coronadite group minerals replace two generations of dolomite while
137 preserving their original texture (Dekoninck et al., 2016a; Fig. 5a). This stage is followed by the neoformation of
138 K-Mn oxides in open spaces (stage 2), forming colloform concretions of hollandite alongside pyrolusite beds
139 (Dekoninck et al. 2016a) (Figs. 5b-c). Intense brecciation is observed and is related to the late stage crystallization
140 of Mn oxides and calcite (Dekoninck et al., 2016b; Gutzmer et al., 2006; Figs. 4 and 5b-c). Romanechite
141 [(Ba,H₂O)₂Mn₅O₁₀], lithiophorite [(Al,Li)MnO₂(OH)₂] and goethite are accessory minerals (Dekoninck et al.
142 2016a), the latter being present in the northwestern part of the Imini area (Bouladon and Jouravsky 1952; Pouit
143 1964). Goethite occurs before the Mn oxides (Fig. 4) and has been dated between ca. 80 to ca. 50 Ma (Verhaert
144 et al. 2022). The association of these oxides with dissolution features confirms the karst-hosted model for the
145 Imini deposits (Gutzmer et al. 2006). Gutzmer et al. (2006) reported that Senonian sediments filled karst cavities
146 and were not affected by Mn mineralization.

147 2. Sampling and analytical procedure

148 2.1. ⁴⁰Ar/³⁹Ar geochronology

149 Potassium-bearing Mn oxides have been collected from six sampling sites, from east to west (Fig. 2a): Bou
150 Aguioun (6), Timkit (4), Lantenois (3), Tiffersine (5), Far West (1) and Plateau (1). At Tiffersine, the analyzed
151 K-Mn oxides coat colloform goethite (Fig. 5c)(Table 2).

152 Coronadite group minerals have been collected in the three *stratabound* orebodies (C1, C2 and C3) or in connected
153 stockwork mineralization (Fig. 2b; Table 1). All dated minerals belong to the second stage of Mn mineralization
154 (Figs. 4 and 5; Dekoninck *et al.*, 2016b, 2016a). None of these samples comes from internal karstic sediments.
155 The dated coronadite group mineral samples form several micrometric bands (Figs. 5a-d), consisting of
156 micrometric needles (1µm in diameter and 3–500µm long; Figs. 5b and d; Dekoninck et al., 2016a) growing at
157 the surface of the first epigenetic mineralization stage (Fig. 5d). Potassium contents in these samples, based on
158 EDS and ICP-MS analyses (Dekoninck *et al.*, 2016b), range from 0.43 wt. % to 4.88 wt. % K₂O. The inner (C)
159 and outer (EX) parts of two colloform aggregates were investigated in order to estimate the growth rates (IM98
160 and ECH-101-b; Fig. 5b). Five experiments were duplicated (18TIF02, 18TIF03, IM41d, ECH-101-b-C and ECH-
161 101-b-EX). Pyrolusite belongs to the second stage of mineralization (Figs. 4 and 5d). Quartz and dolomite grains

162 are occasionally disseminated in the Mn oxides (Fig. 5a and d). Late calcite veins cut across Mn oxides (Figs. 5a,
163 c and d). The texture and composition of the K-Mn oxides were checked using a JEOL 6010 LV and 7500-F
164 Scanning Electron Microscopes (SEM) coupled with an ULTRA MINI-CUP Energy Dispersive Spectrometer
165 (EDS) at the Microscopy Service of the University of Namur. $^{40}\text{Ar}/^{39}\text{Ar}$ analyses were performed on single
166 millimeter-scale fragments of Mn oxides using a CO_2 laser probe coupled to a MAP215 mass spectrometer. Details
167 of the $^{40}\text{Ar}/^{39}\text{Ar}$ methodology are in electronic supplementary material (ESM S1). The ages are summarized in
168 Table 1. Raw data are available in ESM S3.

169 **2.2. Lead isotope geochemistry**

170 Lead isotope were analysed on thirty-seven whole rock samples at the Laboratoire G-Time (Université Libre de
171 Bruxelles, ULB, Belgium) with a Plasma II HR-Multi-Collector Inductively Coupled Plasma Mass Spectrometer
172 (Nu Instruments). These include: (i) the Neoproterozoic volcanic and plutonic basement rocks of the northern
173 Anti-Atlas, (ii) the late Neoproterozoic Mn vein deposits of the northern Anti-Atlas, (iii) the Cambrian basalts,
174 (iv) the Cambrian-Ordovician shales of the Atlas, (v) the Triassic CAMP basalts and interbedded red evaporitic
175 sandstones, (vi) the CT dolostone hosting the Tasdremt and Imini Mn mineralization and (vii) the Mn ores of the
176 Imini and Tasdremt areas. We have collected the least altered samples in outcrops but basalts were subjected to
177 alteration/weathering. We additionally leached basalt samples (Triassic and Cambrian) to avoid any
178 alteration/weathering effects on the pristine isotopic signatures (ESM S2). See ESM S1 for analytical details and
179 ESM S4 for geochemistry of the samples.

180 **3. Results**

181 **3.1. $^{40}\text{Ar}/^{39}\text{Ar}$ dating**

182 The complex age spectra obtained in this study reflect the coexistence of several radiogenic components of
183 different ages in the samples analysed. This may be at the origin of many geologically significant ages. A detailed
184 analysis of the $^{40}\text{Ar}/^{39}\text{Ar}$ data, based on the works of Vasconcelos et al. (1995, 1999), Ruffet et al. (1996),
185 Hénocque et al. (1998), Colin et al. (2005), Beauvais et al. (2008), De Putter et al. (2015) and De Putter and Ruffet
186 (2020), is therefore essential to detect, identify and possibly validate these radiogenic components.

187 The age spectra of two samples from the Timkit site (IM37 and IM39), which have very pronounced saddle shapes
188 (Fig. 8g-h), have to be rejected. The convex trajectory of the degassing steps in the inverse isochron diagram
189 reflects an intense recoil of $^{39}\text{Ar}_K$ during irradiation. The presence of a contaminant or inherited component cannot
190 be excluded.

191 With the exception of samples IM98-EX, 18TIF03 or 18TIF13, all age spectra show abnormally high apparent
192 ages in the low temperature steps, which rapidly decrease in the first 20% of $^{39}\text{Ar}_K$ degassing (Figs. 6, 7, 8 and 9).
193 Their possible significances, not relevant to this study, have been discussed in detail by Dekoninck et al. (2021).
194 Three groups of $^{40}\text{Ar}/^{39}\text{Ar}$ analyses can be distinguished allowing the identification of three radiogenic
195 components: (i) late Cretaceous to early Paleogene, (ii) Priabonian and (iii) Burdigalian-Serravalian (Table 1).
196 We first present the Priabonian age group because it provides crucial information for the characterisation of the
197 other two .

198 ***3.1.1. Priabonian radiogenic component***

199 This group (Fig. 6) consists of Mn oxides growing on goethite (Fig. 5c). Samples were collected in the C3 orebody
200 at Tiffersine (18TIF03, 05 & 12) and from the Plateau site (18PL12b; Fig. 2a). $^{40}\text{Ar}/^{39}\text{Ar}$ experiments are
201 characterized by (i) $^{37}\text{Ar}_{\text{Ca}}/^{39}\text{Ar}_K$ ratios in the range of 0.5-2 (Fig. 6b-e), significantly higher than those of the other
202 samples from this study, (ii) high atmospheric contamination rates and (iii) low K-content. The main radiogenic
203 component is Priabonian in age as shown by the plateau age at 36.3 ± 1.1 Ma (Fig. 6c).

204 The Priabonian radiogenic component is neither the oldest nor the youngest in the analysed samples (Fig. 6a). The
205 low to medium temperature steps of one of the age spectra of sample 18TIF03 (Fig. 6a), and the age spectrum of
206 sample 18TIF12 (Fig. 6d) give pseudo-plateau ages at 35.6 ± 1.8 Ma, and 35.5 ± 0.9 Ma, respectively.
207 Nonetheless, the high temperature steps with apparent ages as old as ca. 51 Ma suggest that the Priabonian
208 component is superimposed on an older one (Fig. 6d), likely to be Paleocene to late Cretaceous in age. A younger
209 component is also superimposed on the Priabonian component. This is observed in the steady increase in apparent
210 ages of the second age spectrum from sample 18TIF03 (Fig. 6b). This feature is characteristic of supergene K-Mn
211 oxides, when two distinct age phases co-exist (De Putter et al., 2015). This age spectrum provides an overestimate
212 of the age of the youngest component ($< \text{ca. } 24.1$ Ma), possibly of Miocene age, as well as an underestimate of
213 the age of the oldest component ($> \text{ca. } 33.9$ Ma), possibly of Priabonian age. At the same time, the $^{37}\text{Ar}_{\text{Ca}}/^{39}\text{Ar}_K$
214 ratios increase from ca.0.8 to ca.1.8, confirming the increasing input of a Ca-rich component, in line with the
215 Priabonian component. The Miocene disturbance is also highlighted by analysis of sample 18PL12b (Fig. 6e).
216 The low to medium temperature steps define a pseudo-plateau at 14.3 ± 0.1 Ma, which is not validated by the
217 isochron calculation [$^{36}\text{Ar}/^{40}\text{Ar}$ vs. $^{39}\text{Ar}_K/^{40}\text{Ar}_K$; Hanes et al., 1985; Roddick et al., 1980; Turner, 1971 -
218 Atmospheric ratio $^{40}\text{Ar}/^{36}\text{Ar} = 298.56$ according to Lee et al. (2006)]. The high temperature steps allow the
219 calculation of a pseudo-plateau age of 36.8 ± 0.6 Ma. The age and $^{37}\text{Ar}_{\text{Ca}}/^{39}\text{Ar}_K$ spectra have similar shapes. The

220 increase in $^{37}\text{Ar}_{\text{Ca}}/^{39}\text{Ar}_{\text{K}}$ ratios during degassing, from ca. 0.1 to ca. 0.9, highlights the Ca-rich signature of the
221 high temperature radiogenic component (Fig. 6e). This is consistent with what is expected for the Priabonian
222 component. The frequency histogram (probability density diagram) of the apparent ages (Fig. 6a) synthesizes
223 information about the Priabonian component.

224 *3.1.2. Miocene radiogenic component*

225 Samples IM98, ECH101b, ECH102b, ECH103 and ECH104, collected in the C1 horizon and the stockwork of
226 the Bou Aguioun area, as well as samples 18TIF02 and 18TIF13 collected from the C3 horizon of the Tiffersine
227 area (Figs. 2a and 7b-h) have dominant Miocene radiogenic components. Most of them have $^{37}\text{Ar}_{\text{Ca}}/^{39}\text{Ar}_{\text{K}}$ ratios
228 in the range 0.001-0.1.

229 The Miocene radiogenic components span a period of ca. 7 Myr, between ca. 20 Ma and ca.13 Ma, from
230 Burdigalian to early Serravallian periods. Their ages depend on the sampling areas. In the Bou Aguioun area (C1
231 and stockwork mineralization) (Fig. 7b-d, g-h; Table 1), the samples yield mostly early Burdigalian ages in the
232 range 19–20 Ma with 5 plateau ages supported by the isochron calculation.

233 In contrast, the outer (EX) domain of the IM98 colloform aggregate (Fig. 7b) yields an apparent plateau age at
234 15.0 ± 0.1 Ma, which is ca. 4.7 Ma younger than the inner domain (IM98-C; Fig. 5b). Although validated by
235 isochron calculation, the subtle hump shape of the age spectrum of IM98-EX indicates mixing between two
236 radiogenic components of different ages (Wijbrans and McDougall 1986; Ruffet et al. 1996; Vasconcelos 1999;
237 Beauvais et al. 2008). The older component is mostly expressed in the middle temperature domain of the age
238 spectrum and would be older than ca. 15 Ma, whereas the secondary component, whose influence is perceptible
239 in the low and high temperature steps, is younger than ca. 14 Ma. This attempt to evaluate the duration of
240 precipitation is unsuccessful. Duplicate analyses of the ca. 15mm colloform aggregate ECH101-b (Fig. 7h) show
241 that there are no significant differences between the age of the core (C) and the outer rim (EX). All age spectra
242 define a frequency peak of apparent ages at ca. 19.3 - 20.5 Ma (Fig. 7h).

243 Samples 18TIF02 and 18TIF13 collected at Tiffersine in the C3 orebody (Figs. 2 and 7e-f) provide contrasting
244 data to those previously mentioned, both in terms of age spectra shape and apparent ages. Sample 18TIF02 (Fig.
245 6e) yields a flat age spectrum (no plateau) with a mean age at 16.0 ± 0.1 Ma which is not validated by the isochron
246 calculation. The two other age spectra from sample 18TIF02 show staircase shapes with apparent ages that
247 increase up to ca. 26.5 Ma. The flat low temperature steps of samples 18TIF02 and 18TIF13 yield two concordant
248 pseudo-plateau ages at 13.0 ± 0.3 Ma and 13.1 ± 0.3 Ma, respectively. The degassing peak associated with the

249 pseudo-plateau of sample 18TIF02 shows that a mineral component would have crystallized in the early
250 Serravallian (ca. 13 Ma) (Fig. 7e-f). Its radiogenic component is characterized by $^{37}\text{Ar}_{\text{Ca}}/^{39}\text{Ar}_{\text{K}}$ (#Ca/K) ratios in
251 the range of 0.001-0.1. It is also superimposed on a Ca-rich ($^{37}\text{Ar}_{\text{Ca}}/^{39}\text{Ar}_{\text{K}}$ ratios in range 0.1-1) and older (> ca.
252 26.5 Ma) radiogenic components (probably Priabonian). We observe the same effect in the high temperature steps
253 for sample ECH101-b (core) (Fig. 7h). The $^{37}\text{Ar}_{\text{Ca}}/^{39}\text{Ar}_{\text{K}}$ ratios in range 0.1-1 throughout the degassing spectrum
254 of sample 18TIF13 (Fig. 7f) suggest that the pseudo-plateau age at ca.17.4 Ma may be a mixture between the
255 Serravalian and Priabonian radiogenic components.

256 Although sampling may introduce statistical bias, the results show that there are two distinct radiogenic
257 components: Burdigalian and Serravallian. Detailed data processing suggests that apparent “intermediate” ages in
258 the range ca.14.3-17.4 Ma have no geological significance (Fig. 7a). The Burdigalian radiogenic component is
259 only observed in the C1 horizon and in the Bou Aguioun stockwork mineralization, whereas the Serravalian
260 radiogenic component is predominantly observed in the C3 horizon at Tiffersine (Fig. 7a) and Plateaux sites (Fig.
261 6a).

262 ***3.1.3. Late Cretaceous (to early Paleogene?) radiogenic components***

263 Age spectra (Fig. 8b-h) from samples from C1-C2 at Timkit (IM36, IM37, IM39 and IM40), C2 at Bou Aguioun
264 (18BA01) and C3 orebodies at the Far West (IM41d) and Lantenois sites (LAN18, LAN57 and LAN59) can be
265 interpreted in the light of the geochronological study of the late Cretaceous mineralization of the Tasdremt Mn
266 district (Dekoninck et al., 2021). These authors have identified four radiogenic components: (i) Turonian (ca. 91.5
267 Ma), (ii) Campanian (ca. 82 Ma to ca. 77.5 Ma), (iii) Late Maastrichtian (ca. 67-65 Ma) and (iv) Late Paleocene
268 (ca.58 Ma). The age spectra (Fig. 8b-f) display a staircase shape. This indicates mixing of two radiogenic
269 components: a secondary component in the low-temperature domain is superimposed on a primary component
270 that degasses at higher temperatures. The apparent or pseudo-plateau ages in the low- and high temperature steps
271 provide over- and underestimates of the ages of the secondary component and the primary component,
272 respectively (Fig. 8b-f). Not all samples in this group are comparable. The primary and secondary components
273 are unlikely to be unique, and there may be several disturbances superimposed on the same sample (Fig. 8a) as
274 observed by Dekoninck et al. (2021). We distinguish two subgroups.

275 (1) In samples IM36 and IM40 (C1-C2 Timkit; Fig. 8d-e), the primary component could be at least as old as
276 ca.66.6 Ma, comparable to the Late Maastrichtian component identified by Dekoninck et al (2021). Two later
277 disturbances are identified by two degassing peaks in the low to mid-temperature domain of the IM36 degassing

278 spectrum. They are superimposed on the early degassing domain of the primary component (Fig.8d). The first
279 disturbance is thought to have occurred around ca. 59 Ma and may be comparable to the Late Paleocene
280 component identified in the Tasdremt district (Dekoninck et al. 2021). The second event is thought to have
281 occurred after ca. 54.7 Ma. Analysis of sample IM40 (Fig. 8e) suggests that this disturbance is younger than ca.
282 47 Ma and could be related to the Priabonian and Miocene radiogenic components.

283 (2) The flat high temperature segments of the age spectra of samples collected in the C3 ore at Lantenois (LAN18,
284 57 and 59)(Fig. 8c, g), Far West (IM41d)(Fig. 8b), and in the C2 at Bou Aguioun (18BA01)(Fig. 8h), suggest that
285 the primary component is at least as old as ca. 80 Ma. It is comparable to the Campanian component identified at
286 Tasdremt (Dekoninck et al. 2021). The apparent ages or small segments identified in the low temperature steps,
287 in the range ca. 61.6-69.3 Ma, suggest that the secondary component could be of middle Paleocene in age.

288 **3.2. Pb isotope compositions**

289 The Pb isotopic ratios vary from 17.266 to 28.263 ($^{206}\text{Pb}/^{204}\text{Pb}$), 15.437 to 16.122 ($^{207}\text{Pb}/^{204}\text{Pb}$), 37.571 to 43.688
290 ($^{208}\text{Pb}/^{204}\text{Pb}$; Fig. 9; ESM S2). They have been recalculated to take into account the age of the primary ore
291 deposition at 67 Ma (Figs. 9a- b)(Dekoninck et al. 2021). It implies slight changes of the recalculated $^{206}\text{Pb}/^{204}\text{Pb}$
292 and $^{207}\text{Pb}/^{204}\text{Pb}$ ratios up to 0.673 and 0.032, respectively, from the measured ratios. The significant changes of
293 the recalculated $^{208}\text{Pb}/^{204}\text{Pb}$ ratios up to 90.711 is due to samples having high Th/Pb ratio that brings more
294 radiogenic ^{208}Pb . We do not report the recalculated $^{208}\text{Pb}/^{204}\text{Pb}$ ratios. However, the $^{206}\text{Pb}/^{204}\text{Pb}$ vs $^{208}\text{Pb}/^{204}\text{Pb}$ and
295 $^{207}\text{Pb}/^{204}\text{Pb}$ vs $^{208}\text{Pb}/^{204}\text{Pb}$ are compiled and are reported in ESM S6; they show the same trends defined in Figure
296 9 and do not bring additional value to the following interpretations.

297 The Pb isotopic compositions of the Imini Mn ores cluster in a narrow $^{206}\text{Pb}/^{204}\text{Pb}$ range of 18.614-18.772,
298 $^{207}\text{Pb}/^{204}\text{Pb}$ 15.619-15.678 and $^{208}\text{Pb}/^{204}\text{Pb}$ range of 38.530-39.229. These data are significantly different from
299 those of Mn ore veins of Bachkoun and Tiouine hosted in Neoproterozoic volcanic rocks and other Neoproterozoic
300 mineralization (Bouabdellah et al. 2016; Figs. 9a-b).

301 Neoproterozoic rhyolite and andesite of the Ouarzazate Supergroup display a wide range of more radiogenic
302 isotopic ratios: ($^{206}\text{Pb}/^{204}\text{Pb}$) 7.173-24.921 , ($^{207}\text{Pb}/^{204}\text{Pb}$) 20.053-28.263 and $^{208}\text{Pb}/^{204}\text{Pb}$ 15.663-16.122. The
303 Neoproterozoic granite and granodiorite have different isotopic compositions; sample 15TAG02 has Pb isotopic
304 ratios falling in the range of the Neoproterozoic volcanic rocks, ($^{206}\text{Pb}/^{204}\text{Pb}$) 15.658, ($^{207}\text{Pb}/^{204}\text{Pb}$) 20.213 and
305 $^{208}\text{Pb}/^{204}\text{Pb}$ 38.313, whereas ASK02 has the least radiogenic signature with values of ($^{206}\text{Pb}/^{204}\text{Pb}$) 17.266
306 ,($^{207}\text{Pb}/^{204}\text{Pb}$) 15.437 and $^{208}\text{Pb}/^{204}\text{Pb}$ 38.041.

307 The CAMP Triassic basalts are characterized by a wider range of isotopic compositions: ($^{206}\text{Pb}/^{204}\text{Pb}$) 15.612-
308 15.712 , ($^{207}\text{Pb}/^{204}\text{Pb}$) 18.435-19.638 and $^{208}\text{Pb}/^{204}\text{Pb}$ 21.879-38.178 , similar to those obtained by Marzoli et al.
309 (2019) for the Atlas belt (Figs. 9a-b). Leached basalt samples plot in a narrow field due to removing of the
310 alteration/weathering minerals (Fig. 9c). They have a different isotopic composition than Triassic basalts with
311 ($^{206}\text{Pb}/^{204}\text{Pb}$) 18.267 and ($^{207}\text{Pb}/^{204}\text{Pb}$) 15.641.

312 The Triassic sandstone sample overlaps the isotopic field of the Mn ore ($^{206}\text{Pb}/^{204}\text{Pb}$ 18.824, $^{207}\text{Pb}/^{204}\text{Pb}$ 15.668,
313 $^{208}\text{Pb}/^{204}\text{Pb}$ 38.820;). The CT dolostone samples overlap the compositional field basalts and the Mn ore samples
314 ($^{206}\text{Pb}/^{204}\text{Pb}$ 18.472-18.692, $^{207}\text{Pb}/^{204}\text{Pb}$ 15.610-15.663, $^{208}\text{Pb}/^{204}\text{Pb}$ 38.255-38.647;). The Ordovician shale of the
315 Imini anticline ($^{206}\text{Pb}/^{204}\text{Pb}$ 18.772, $^{207}\text{Pb}/^{204}\text{Pb}$ 15.678, $^{208}\text{Pb}/^{204}\text{Pb}$ 39.229;) has a significantly different isotopic
316 composition than Ordovician shales of the High Atlas ($^{206}\text{Pb}/^{204}\text{Pb}$ 20.565-20.643, $^{207}\text{Pb}/^{204}\text{Pb}$ 15.817-15.839,
317 $^{208}\text{Pb}/^{204}\text{Pb}$ 43.514-43.688;)(Figs. 9a- b).

318 4. Discussion

319 4.1. Source rocks for the metals

320 Among potential source rocks, the CT dolostone displays the most similar Pb isotopic compositions to the Imini
321 Mn ore. These rocks cannot be considered as the source of metals given the low primary Mn-Ba-K-Pb content
322 and their narrow thickness (Dekoninck et al. 2016b). Their Pb isotope composition can be impacted by
323 disseminated Mn oxides (Gutzmer et al. 2006; Dekoninck et al. 2016a) that may overprint the pristine Pb isotope
324 of the dolostone. This is supported by slight enrichments in Mn, Ba and Pb in some dolostone samples (see ESM
325 S4). This similar Pb isotope composition can also be due to fluid-rock interaction with the fluid that precipitated
326 the Mn oxides in the host dolostone. A similar pattern is observed in Ordovician shales in contact with the Mn ore
327 that have similar $^{206}\text{Pb}/^{204}\text{Pb}$ and $^{207}\text{Pb}/^{204}\text{Pb}$ ratios as the Mn ores, whereas samples away from the district show
328 a Pb compositions different from that of Mn ore (Fig. 9a).

329 Triassic CAMP basalts and interlayered red sandstones are voluminous along the Atlas range of Morocco (Marzoli
330 et al. 2019) and are a likely source for the Mn mineralization. Both rock types fall in the same isotopic field as the
331 Mn ore (Fig. 9b). Locally, basalts show a siliceous alteration characterized by clays, chayasite, quartz-jasper (ESM
332 S7) and a higher dispersion to of their $^{206}\text{Pb}/^{204}\text{Pb}$ and $^{207}\text{Pb}/^{204}\text{Pb}$ ratios (Fig. 9c). These basalts typically have low
333 Mn (0.07-0.47 wt.%; avg. 0.18 wt.% MnO), Ba (53-430 ppm; avg. 190 ppm Ba; 0.05), K (0.21-1.68 wt.%; avg.
334 0.68 wt.% K_2O) and particularly for Pb (2-58 ppm; avg. 4 ppm Pb; SDR1; Marzoli et al., 2019) contents. Given
335 their similar Pb isotope composition (Fig. 9), the red sandstone is likely a second source of metals with basalts

336 (Fig. 9). Therefore, the source of metals is Triassic and is located in the Atlas, which is crucial to understand the
337 significance of the $^{40}\text{Ar}/^{39}\text{Ar}$ ages.

338 **4.2. The Imini ore deposit: a ~90 My multistage history**

339 The $^{40}\text{Ar}/^{39}\text{Ar}$ geochronological study shows three significant periods of Mn deposition/remobilization: late
340 Cretaceous (-Middle Paleocene) (ca. >59 Ma), Priabonian (ca. 36.3 Ma) and Burdigalian-Serravalian (ca. 19–20
341 Ma and ca. 13 Ma, Table 1 and Figs. 6, 7 and 8). There is no age difference between the stratabound and stockwork
342 mineralization, which suggest that they were likely formed together. The relative time frame established by
343 Dekoninck et al. (2016a) shows that most of the pyrolusite postdates the dated K-Mn oxides (Fig. 4). Even if
344 pyrolusite is likely connected to stage 2 open space filling rather than stage 1 (Figs. 4, 5a and d), it means that
345 $^{40}\text{Ar}/^{39}\text{Ar}$ ages document only a segment of the entire petrogenetic history.

346 K-bearing Mn oxides are complex materials able to register several mineralization events at the grain scale. Each
347 event is able to completely or partially erase the previous stage(s)(De Putter and Ruffet 2020). Our $^{40}\text{Ar}/^{39}\text{Ar}$
348 geochronological study draws the same conclusion. Although the age of the initial stage of mineralization is
349 imprecise, we identify at Imini two sub-stages that appear to be contemporaneous with the stage 2 (~77.5–82 Ma)
350 and 3 (~65–67 Ma) observed at Tasdremt by Dekoninck et al. (2021). These authors also identified early stage 1
351 of Turonian age (~91.5 Ma) in this area. Verhaert et al. (2022) report at Imini goethite (U-Th)/He ages as old as
352 92.7 ± 4.6 Ma which suggest that Mn oxide precipitation may have occurred at the same time. The identical
353 petrographic features (Dekoninck et al. 2016a, 2021) and Pb isotope composition of the Mn ores (Fig. 9b) at
354 Tasdremt and Imini argue for a contemporaneous Cretaceous age. However, considering the complexity of the K-
355 Mn oxide $^{40}\text{Ar}/^{39}\text{Ar}$ data at Imini (Figs. 6, 7 and 8), it is likely that some goethite ages of Verhaert et al. (2022),
356 in the range 80-50 Ma, are mixtures of different radiogenic components.

357 At Tasdremt, where pyrolusite is absent and the Mn grade is low, the Mn ore deposition occurred only in the late
358 Cretaceous (Fig. 1b)(Dekoninck et al. 2021), when, at Imini, the high-grade Mn deposit resulted from a multistage
359 depositional history spanning from the late Cretaceous to the Neogene (Fig. 10). The causes of this different
360 evolution remain speculative but could be related to the erosion of the Triassic Mn source, or alternatively by a
361 different hydrodynamic regime. The duration of these processes highlights the importance of time in creating
362 high-grade karst-hosted deposits.

363 **4.3. Relationship between the Imini Mn ore and Atlasic tectonic**

364 From the Cretaceous to the present day, four periods of tectonic activity have built the High Atlas. Our results
365 show that three of these four periods correlate with the K-Mn oxide ages in the Imini Mn district (Fig. 10): the
366 late Cretaceous – Late Paleocene (four sub-phases at ~91.5 Ma, ~77.5–82 Ma, ~65–67 Ma and ~ 58–61.5 Ma),
367 the Late Eocene (ca. 36.3 Ma) and the Early to Middle Miocene (ca. 19–20 Ma and ca.13 Ma). Although the
368 timing of some tectonic phases remains debated, the overall correlation between radiometric ages and
369 tectonic/uplift activity, suggests that mineralization was primarily controlled by the geodynamic evolution of the
370 High Atlas. The Quaternary tectonic phase would account for recent or modern mineralization in the Imini area
371 (Dekoninck et al. 2016a)(Fig. 4).

372 High supplies of meteoric water are needed to sustain fluid-rock interactions with the Triassic series, leaching,
373 transport and finally precipitating metals. The required humid conditions make climate a key parameter. The North
374 Africa paleoclimate was supposed to be arid during Mn deposition events (Algouti et al. 1999; El Harfi et al.
375 2001; Mansour et al. 2021; Zammit et al. 2022). However, higher elevated surface can significantly change the
376 Earth's atmospheric circulation and alter the regional climate (Ruddiman et al. 1997). Therefore, uplift of the
377 Atlas can lead to a constant supply of meteoric water, as it is case today (Bell et al. 2022).

378 The building of a significant relief triggers the required hydraulic head (Gutzmer et al. 2006) for the percolation
379 of subsurface fluids. In the Atlas of Morocco, Choulet et al. (2014), Verhaert et al. (2017, 2020) and Bouabdellah
380 et al. (2021), highlighted the primary role of Atlasic tectonic activity in the formation of supergene ore. This study
381 confirms the primary role of regional exhumation in subsurface geological processes, enhancing the advection of
382 mineralizing fluids. According to Gutzmer et al. (2006), Mn mineralization forms from low-temperature (<100°C)
383 hydrothermal events. Goethite hydrogen and oxygen stable isotope data confirm that the mineralizing fluid was
384 likely hot meteoric water that experienced fluid-rock interactions with the host dolostone and other country rocks
385 (Verhaert et al. 2022). These conditions differ from lateritic subaerial systems. The difference is also materialized
386 by high Mn oxides growth rates (>15mm/Myr), unlike those observed in lateritic systems (1-5 mm/Myr; Hénocque
387 et al., 1998). This link between uplift and low-temperature mineralization has been shown in Central Africa
388 (Decrée et al. 2010; De Putter et al. 2015; De Putter and Ruffet 2020), South Africa (Vasconcelos and Carmo
389 2018), India (Beauvais et al. 2016; Bonnet et al. 2016; Jean et al. 2019) and Western Europe (Hautmann and
390 Lippolt 2000; Barbarand et al. 2018; Dekoninck et al. 2019).

391 **4.4. Geodynamic-related model of the high-grade Imini Mn ore system**

392 *4.4.1. The late Cretaceous primary Mn deposition*

393 The earliest Atlasic deformation likely led the Tasdremt to Imini area (Fig. 1b) to emerge above sea level during
394 the late Cretaceous. These low stand reliefs were flooded several times and resulted in the deposition of sediments
395 during the Upper Santonian, for the whole district, and Campanian in the Tasdremt area (Algouti et al. 1999). We
396 consider that the primary karst Mn deposition took place at ~91.5 Ma, ~77.5–82 Ma, ~65–67 Ma and ca. 58–61.5
397 Ma (Dekoninck et al., 2021 and this study) when the CT succession was in the vadose zone in a terrestrial
398 environment. The C3 ore formed across the whole Imini-Tasdremt Mn district. Except for the earliest
399 mineralization at ~91.5 Ma, Mn was deposited under a cover of sediments, preserving the thin CT host rock
400 dolostone from erosion (Figs. 10 and 11).

401 *4.4.2. The Cenozoic enrichment phases*

402 The link between geodynamic events and the $^{40}\text{Ar}/^{39}\text{Ar}$ ages support Mn deposition when mineralizing fluids
403 migrated from the High Atlas relief and fed temporary aquifers in the CT dolostone (vadose environment). By
404 creating a hydrodynamic gradient, meteoric ground water (Verhaert et al. 2022) transported dissolved metals (Mn,
405 Ba and Pb). The massive Mn oxide ore (especially pyrolusite) is associated with discrete ~N70° structures
406 (Leprêtre et al. 2015), which acted as channels responsible for the orientation of the mineralization (Fig. 2a). The
407 porous and partially dissolved dolostone, led low-temperature acidic and reduced groundwater to be buffered and
408 oxidized in a karst environment. Metal precipitation took place where shallow, O₂-rich, and cold meteoric water
409 resident in the karst system mixed with hydrothermal groundwater (Gutzmer et al. 2006). Dekoninck et al. (2016a)
410 have shown that increasing pH due to dolomite dissolution caused precipitation of Mn oxides. In addition, the ore
411 zone is located where Triassic red sandstones and basalts pinch out (Fig. 11). In this geological setting, and under
412 the influence of overpressure Mn-bearing low-T groundwater due to orogenic head (Gutzmer et al. 2006), Mn-
413 rich hydrothermal fluids were forced into the CT dolostone. The Imini fault zone could also act as a preferential
414 drain for mineralization as shown by (i) an eastern zone enriched in pyrolusite (Dekoninck et al. 2016b) and (ii)
415 host of large quantities of barite (Fig. 1b), a mineral also locally observed in the Imini ore (Fig. 4; Dekoninck et
416 al. 2016a) when Ba is also a major element in hollandite.

417 Other Mn deposits hosted in CT carbonate karsts in Tunisia (Jebel Aziza, Gattar Member) display similarities
418 with the Imini-Tasdremt Mn ore belt, as they are located at the transition zone between the Tunisian Atlas and the
419 Saharan platform (Garnit et al. 2020). Mn occurrences in this area have an orientation following a NW-SE
420 direction, also suggesting a structural control of the Mn mineralization (Amouri et al. 1991). These occurrences

421 (and maybe others) indicate that Mn mineralization hosted in dolostones could have a larger extension in Northern
422 Africa.

423 **5. Conclusion**

424 This innovative study combines $^{40}\text{Ar}/^{39}\text{Ar}$ ages of K-bearing Mn oxides with Pb isotope data from Mn ore samples
425 and of potential regional rock sources to better understand the karst-hosted Mn deposits of the Imini district. Lead
426 isotopic data show that the most likely source of the Mn-Ba-K-Pb metal association in Imini were the Triassic
427 series composed of a thick basaltic pile interlayered in red sandstone. The $^{40}\text{Ar}/^{39}\text{Ar}$ ages indicate that primary Mn
428 formation took place in the late Cretaceous during several pulses (~91.5 Ma, ~77.5–82 Ma and ~65–67 Ma) and
429 probably persisted until the early Paleogene (~58 Ma) along a distance of ~100 km from Imini to Tadmret due
430 to uplift/tectonic pulses related to the earliest Atlasic deformation. Manganese enrichment during a second and
431 third events at ca. 36.3 Ma (Priabonian), and ca. 19–20 and ca. 13 Ma (Early-Middle Miocene), respectively, are
432 recorded by pyrolusite-rich mineralization in the Imini Mn district. These data establish that the Mn mineralization
433 formed in response to regional tectonic events - similar to many other sediment-hosted deposits such as
434 Mississippi Valley type and supergene deposits. This correlation highlights the topographic control through
435 tectonic or uplift, associated with humid climate. Ultimately, uplift events controlled (1) the fluid circulation
436 pattern, (2) leaching of the source rocks, (3) precipitation/remobilization of the largest Mn deposit of North Africa.
437 This long lasting (~90 My) multistage evolution formed high-grade Mn deposits. The discrete N70° tectonic
438 structures and the pinch out of Triassic series in front of the Imini district led to the final trap. This study shows
439 that $^{40}\text{Ar}/^{39}\text{Ar}$ dating coupled with Pb isotope data are key methods to build up robust metallogenic models of
440 karst-hosted mineralization, which can apply in the exploration of similar high-grade Mn deposits.

441 **Acknowledgement**

442 We are grateful to all those involved in the field missions carried out between 2012 and 2018. We acknowledge
443 the “Office National des Mines et des Hydrocarbures” (ONHYM) for having shared their logistical and scientific
444 support. We are very grateful to the Imini mine (SACEM) for providing field access and assistance in the field.
445 We are thankful to Prof. M. Essalhi (University Moulay Ismail Errachidia), Th. Mortier (UMons), Z. Pirotte
446 (ULB), B. Saint-Bézar (PSUD) and G. Delpech (PSUD) for field assistance. We appreciate the help of Prof. J.
447 Wouters and Dr. N. Tumanov of the PC2 platform (UNamur) for collecting XRD patterns. We also thank G.
448 Rochez for gathering field pictures and the preparation of sections and sample powders. Co-authors would like to
449 warmly thank Jeroen De Jong for his assistance during the isotopic analyses, and the “Fonds National de la
450 Recherche Scientifique” (FNRS) for funding support in lab instruments. This research used the resources of the
451 Electron Microscopy Service located at the University of Namur (“Plateforme Technologique Morphologie —
452 Imagerie”). This research did not receive any specific grant from funding agencies in the public, commercial, or
453 not-for-profit sectors. We are very grateful to Prof. M. Bouabdellah and Prof. J. Gutzmer for their careful review
454 of the paper, as well as Prof. G. Beaudoin for editing the final version.

455 **Compliance with Ethical Standards**

456 We declare that this work has been directed without competing interests and is the authors own intellectual
457 property.

458 **References**

- 459 Algouti A, Algouti A, Taj-Eddine K (1999) Le Sénonien du Haut Atlas occidental, Maroc:
460 sédimentologie, analyse séquentielle et paléogéographie. *Journal of African Earth Sciences*
461 29:643–658. [https://doi.org/10.1016/S0899-5362\(99\)00121-9](https://doi.org/10.1016/S0899-5362(99)00121-9)
- 462 Amouri M, Bouaziz S, Ennifar S, et al (1991) Le gîte manganésifère du Jebel Aziza (Chaîne des
463 Chotts) : étude de la minéralisation dans son cadre morphostructural et paléogéographique.
464 *Notes du Service Géologique de Tunisie* 58:133–150
- 465 Barbarand J, Bour I, Pagel M, et al (2018) Post-Paleozoic evolution of the northern Ardenne Massif
466 constrained by apatite fission-track thermochronology and geological data. *BSGF - Earth*
467 *Sciences Bulletin* 189:16. <https://doi.org/10.1051/bsgf/2018015>
- 468 Beaudoin B, Lesavre A, Pelissonnier H (1976) Action des eaux superficielles dans le gisement de
469 manganese d'Imini (Maroc). *Bulletin de la Société Géologique de France* 18:95–100.
470 <https://doi.org/10.2113/gssgfbull.S7-XVIII.1.95>
- 471 Beauvais A, Bonnet NJ, Chardon D, et al (2016) Very long-term stability of passive margin
472 escarpment constrained by $^{40}\text{Ar}/^{39}\text{Ar}$ dating of K-Mn oxides. *Geology* 44:299–302.
473 <https://doi.org/10.1130/G37303.1>
- 474 Beauvais A, Ruffet G, Hénocque O, Colin F (2008) Chemical and physical erosion rhythms of the West
475 African Cenozoic morphogenesis: The ^{39}Ar - ^{40}Ar dating of supergene K-Mn oxides. *Journal of*
476 *Geophysical Research* 113:. <https://doi.org/10.1029/2008JF000996>
- 477 Bell BA, Hughes PD, Fletcher WJ, et al (2022) Climate of the Marrakech High Atlas, Morocco:
478 Temperature lapse rates and precipitation gradient from piedmont to summits. *Arctic,*
479 *Antarctic, and Alpine Research* 54:78–95. <https://doi.org/10.1080/15230430.2022.2046897>
- 480 Bonnet NJ, Beauvais A, Arnaud N, et al (2016) Cenozoic lateritic weathering and erosion history of
481 Peninsular India from $^{40}\text{Ar}/^{39}\text{Ar}$ dating of supergene K–Mn oxides. *Chemical Geology*
482 446:33–53. <https://doi.org/10.1016/j.chemgeo.2016.04.018>
- 483 Bouabdellah M, Boukirou W, Potra A, et al (2021) Origin of the Moroccan Touissit-Bou Beker and
484 Jbel Bou Dahar supergene non-sulfide biomineralization and its relevance to microbiological
485 activity, late Miocene uplift and climate changes. *Minerals* 11:401.
486 <https://doi.org/10.3390/min11040401>
- 487 Bouabdellah M, Maacha L, Jébrak M, Zouhair M (2016) Re/Os Age Determination, Lead and Sulphur
488 Isotope Constraints on the Origin of the Bouskour Cu–Pb–Zn Vein-Type Deposit (Eastern
489 Anti-Atlas, Morocco) and Its Relationship to Neoproterozoic Granitic Magmatism. In:
490 Bouabdellah M, Slack JF (eds) *Mineral Deposits of North Africa*. Springer International
491 Publishing, Cham, pp 277–290
- 492 Bouabdellah M, Niedermann S, Velasco F (2015) The Touissit-Bou Beker Mississippi Valley-Type
493 District of Northeastern Morocco: Relationships to the Messinian Salinity Crisis, Late
494 Neogene–Quaternary Alkaline Magmatism, and Buoyancy-Driven Fluid Convection. *Economic*
495 *Geology* 110:1455–1484. <https://doi.org/10.2113/econgeo.110.6.1455>

- 496 Bouabdellah M, Sangster DF, Leach DL, et al (2012) Genesis of the Touissit-Bou Beker Mississippi
497 Valley-Type District (Morocco-Algeria) and Its Relationship to the Africa-Europe Collision.
498 *Economic Geology* 107:117–146. <https://doi.org/10.2113/econgeo.107.1.117>
- 499 Bouladon J, Jouravsky G (1952) Géologie des gites minéraux marocains: Manganèse. Alger, pp 44–80
- 500 Cavallina C, Papini M, Moratti G, Benvenuti M (2018) The late Mesozoic evolution of the Central High
501 Atlas domain (Morocco): Evidence from the paleo-drainage record of the Adrar Aglagal
502 syncline. *Sedimentary Geology* 376:1–17. <https://doi.org/10.1016/j.sedgeo.2018.08.003>
- 503 Choubert G, Faure-Muret A (1973) The Precambrian iron and manganese deposits of the Anti-Atlas.
504 In: *Genesis of Precambrian iron and manganese deposits*. Kiev, pp 115–124
- 505 Choulet F, Charles N, Barbanson L, et al (2014) Non-sulfide zinc deposits of the Moroccan High Atlas:
506 Multi-scale characterization and origin. *Ore Geology Reviews* 56:115–140.
507 <https://doi.org/10.1016/j.oregeorev.2013.08.015>
- 508 Colin F, Beauvais A, Ruffet G, Henocque O (2005) First $^{40}\text{Ar}/^{39}\text{Ar}$ geochronology of lateritic
509 manganiferous pisolites: Implications for the Palaeogene history of a West African
510 landscape. *Earth and Planetary Science Letters* 238:172–188.
511 <https://doi.org/10.1016/j.epsl.2005.06.052>
- 512 Cornée J-J, Destombes J (1991) L'ordovicien de la partie W du massif ancien du Haut-Atlas occidental
513 (Maroc hercynien). *Geobios* 24:403–415. [https://doi.org/10.1016/S0016-6995\(06\)80238-X](https://doi.org/10.1016/S0016-6995(06)80238-X)
- 514 De Putter T, Ruffet G (2020) Supergene manganese ore records 75 Myr-long Campanian to
515 Pleistocene geodynamic evolution and weathering history of the Central African Great Lakes
516 Region – Tectonics drives, climate assists. *Gondwana Research* 83:96–117.
517 <https://doi.org/10.1016/j.gr.2020.01.021>
- 518 De Putter T, Ruffet G, Yans J, Mees F (2015) The age of supergene manganese deposits in Katanga
519 and its implications for the Neogene evolution of the African Great Lakes Region. *Ore
520 Geology Reviews* 71:350–362. <https://doi.org/10.1016/j.oregeorev.2015.06.015>
- 521 Deckart K, Féraud G, Bertrand H (1997) Age of Jurassic continental tholeiites of French Guyana,
522 Surinam and Guinea: Implications for the initial opening of the Central Atlantic Ocean. *Earth
523 and Planetary Science Letters* 150:205–220. [https://doi.org/10.1016/S0012-821X\(97\)00102-7](https://doi.org/10.1016/S0012-821X(97)00102-7)
524 7
- 525 Decrée S, Deloule É, Ruffet G, et al (2010) Geodynamic and climate controls in the formation of Mio–
526 Pliocene world-class oxidized cobalt and manganese ores in the Katanga province, DR Congo.
527 *Mineralium Deposita* 45:621–629. <https://doi.org/10.1007/s00126-010-0305-8>
- 528 Dekoninck A, Bernard A, Barbarand J, et al (2016a) Detailed mineralogy and petrology of manganese
529 oxyhydroxide deposits of the Imini district (Morocco). *Mineralium Deposita* 51:13–23.
530 <https://doi.org/10.1007/s00126-015-0590-3>
- 531 Dekoninck A, Leprêtre R, Saddiqi O, et al (2016b) The high-grade Imini manganese district—karst-
532 hosted deposits of Mn oxides and oxyhydroxides. In: Bouabdellah M, Slack JF (eds) *Mineral
533 Deposits of North Africa*. Springer International Publishing, Cham, pp 575–594
- 534 Dekoninck A, Monié P, Blockmans S, et al (2019) Genesis and $^{40}\text{Ar}/^{39}\text{Ar}$ dating of K-Mn oxides from
535 the Stavelot Massif (Ardenne, Belgium): Insights into Oligocene to Pliocene weathering

536 periods in Western Europe. *Ore Geology Reviews* 115:103–191.
537 <https://doi.org/10.1016/j.oregeorev.2019.103191>

538 Dekoninck A, Ruffet G, Missenard Y, et al (2021) Multistage genesis of the late Cretaceous
539 manganese karst-hosted Tasdremt deposit (High Atlas, Morocco). *Mineralium Deposita*
540 59:935–956. <https://doi.org/10.1007/s00126-020-01017-0>

541 El Arabi EH, Diez JB, Broutin J, Essamoud R (2006) Première caractérisation palynologique du Trias
542 moyen dans le Haut Atlas ; implications pour l’initiation du rifting téthysien au Maroc.
543 *Comptes Rendus Geoscience* 338:641–649. <https://doi.org/10.1016/j.crte.2006.04.001>

544 El Harfi A, Lang J, Salomon J, Chellai E (2001) Cenozoic sedimentary dynamics of the Ouarzazate
545 foreland basin (Central High Atlas Mountains, Morocco). *Int J Earth Sci* 90:393–411.
546 <https://doi.org/10.1007/s005310000115>

547 Fekkak A, Ouanaïmi H, Michard A, et al (2018) Thick-skinned tectonics in a Late Cretaceous-Neogene
548 intracontinental belt (High Atlas Mountains, Morocco): The flat-ramp fault control on
549 basement shortening and cover folding. *Journal of African Earth Sciences* 140:169–188.
550 <https://doi.org/10.1016/j.jafrearsci.2018.01.008>

551 Frizon de Lamotte D, Leturmy P, Missenard Y, et al (2009) Mesozoic and Cenozoic vertical
552 movements in the Atlas system (Algeria, Morocco, Tunisia): An overview. *Tectonophysics*
553 475:9–28. <https://doi.org/10.1016/j.tecto.2008.10.024>

554 Frizon de Lamotte D, Saint Bezar B, Bracène R, Mercier E (2000) The two main steps of the Atlas
555 building and geodynamics of the western Mediterranean. *Tectonics* 19:740–761.
556 <https://doi.org/10.1029/2000TC900003>

557 Frizon de Lamotte D, Zizi M, Missenard Y, et al (2008) The Atlas System. In: Michard A, Saddiqi O,
558 Chalouan A, Lamotte DF de (eds) *Continental Evolution: The Geology of Morocco*. Springer
559 Berlin Heidelberg, Berlin, Heidelberg, pp 133–202

560 Froitzheim N (1984) Late Cretaceous vertical tectonics in the High Atlas SW of Marrakech/Morocco -
561 Reconstruction of tectonic movements in an early stage of the High Atlas orogenesis. *Neu Jb*
562 *Paläont Mh* 463–471

563 Froitzheim N, Stets J, Wurster P (1988) Aspects of Western High Atlas tectonics. In: Jacobshagen VH
564 (ed) *The Atlas System of Morocco*. Springer-Verlag, Berlin/Heidelberg, pp 219–244

565 Fullea J, Fernández M, Afonso JC, et al (2010) The structure and evolution of the lithosphere–
566 asthenosphere boundary beneath the Atlantic–Mediterranean Transition Region. *Lithos*
567 120:74–95. <https://doi.org/10.1016/j.lithos.2010.03.003>

568 Garnit H, Kraemer D, Bouhlel S, et al (2020) Manganese ores in Tunisia: Genetic constraints from
569 trace element geochemistry and mineralogy. *Ore Geology Reviews* 120:103451.
570 <https://doi.org/10.1016/j.oregeorev.2020.103451>

571 Gasquet D, Levresse G, Cheilletz A, et al (2005) Contribution to a geodynamic reconstruction of the
572 Anti-Atlas (Morocco) during Pan-African times with the emphasis on inversion tectonics and
573 metallogenic activity at the Precambrian–Cambrian transition. *Precambrian Research*
574 140:157–182. <https://doi.org/10.1016/j.precamres.2005.06.009>

- 575 Groves DI, Bierlein FP (2007) Geodynamic settings of mineral deposit systems. *Journal of the*
576 *Geological Society* 164:19–30. <https://doi.org/10.1144/0016-76492006-065>
- 577 Gutzmer J, Beukes NJ, Rhalmi M, Mukhopadhyay J (2006) Cretaceous karstic cave-fill manganese-
578 lead-barium deposits of Imini, Morocco. *Economic Geology* 101:385–405.
579 <https://doi.org/10.2113/gsecongeo.101.2.385>
- 580 Hanes JA, York D, Hall CM (1985) An $^{40}\text{Ar}/^{39}\text{Ar}$ geochronological and electron microprobe
581 investigation of an Archaean pyroxenite and its bearing on ancient atmospheric
582 compositions. *Canadian Journal of Earth Sciences* 22:947–958. [https://doi.org/10.1139/e85-](https://doi.org/10.1139/e85-100)
583 100
- 584 Hautmann S, Lippolt HJ (2000) $^{40}\text{Ar}/^{39}\text{Ar}$ dating of central European K–Mn oxides — a chronological
585 framework of supergene alteration processes during the Neogene. *Chemical Geology*
586 170:37–80. [https://doi.org/10.1016/S0009-2541\(99\)00241-7](https://doi.org/10.1016/S0009-2541(99)00241-7)
- 587 Hénocque O, Ruffet G, Colin F, Féraud G (1998) $^{40}\text{Ar}/^{39}\text{Ar}$ dating of West African lateritic
588 cryptomelanes. *Geochimica et Cosmochimica Acta* 62:2739–2756.
589 [https://doi.org/10.1016/S0016-7037\(98\)00185-9](https://doi.org/10.1016/S0016-7037(98)00185-9)
- 590 Herbig H-G (1988) Synsedimentary tectonics in the Northern Middle Atlas (Morocco) during the late
591 Cretaceous and Tertiary. In: Jacobshagen VH (ed) *The Atlas system of Morocco: studies on its*
592 *geodynamic evolution*. Springer Berlin Heidelberg, Berlin, Heidelberg, pp 321–337
- 593 Jean A, Beauvais A, Chardon D, et al (2019) Weathering history and landscape evolution of Western
594 Ghats (India) from $^{40}\text{Ar}/^{39}\text{Ar}$ dating of supergene K–Mn oxides. *Journal of the Geological*
595 *Society*. <https://doi.org/10.1144/jgs2019-048>
- 596 Lanari R, Fellin MG, Faccenna C, et al (2020) Exhumation and Surface Evolution of the Western High
597 Atlas and Surrounding Regions as Constrained by Low-Temperature Thermochronology.
598 *Tectonics* 39:e2019TC005562. <https://doi.org/10.1029/2019TC005562>
- 599 Lanari R, Reitano R, Giachetta E, et al (2022) Is the Anti-Atlas of Morocco still uplifting? *Journal of*
600 *African Earth Sciences* 188:104481. <https://doi.org/10.1016/j.jafrearsci.2022.104481>
- 601 Landing E, Bowring SA, Davidek KL, et al (1998) Duration of the Early Cambrian: U–Pb ages of volcanic
602 ashes from Avalon and Gondwana. *Can J Earth Sci* 35:329–338. [https://doi.org/10.1139/e97-](https://doi.org/10.1139/e97-107)
603 107
- 604 Laznicka P (2014) Giant metallic deposits—A century of progress. *Ore Geology Reviews* 62:259–314.
605 <https://doi.org/10.1016/j.oregeorev.2014.03.002>
- 606 Lee J-Y, Marti K, Severinghaus JP, et al (2006) A redetermination of the isotopic abundances of
607 atmospheric Ar. *Geochimica et Cosmochimica Acta* 70:4507–4512.
608 <https://doi.org/10.1016/j.gca.2006.06.1563>
- 609 Leprêtre R, Missenard Y, Barbarand J, et al (2018) Polyphased inversions of an intracontinental rift:
610 case study of the Marrakech High Atlas, Morocco. *Tectonics* 37:818–841.
611 <https://doi.org/10.1002/2017TC004693>
- 612 Leprêtre R, Missenard Y, Saint-Bezar B, et al (2015) The three main steps of the Marrakech High Atlas
613 building in Morocco: Structural evidences from the southern foreland, Imini area. *Journal of*
614 *African Earth Sciences* 109:177–194. <https://doi.org/10.1016/j.jafrearsci.2015.05.013>

- 615 Lippolt HJ, Hautmann S (1995) $^{40}\text{Ar}/^{39}\text{Ar}$ ages of Precambrian manganese ore minerals from Sweden,
616 India and Morocco. *Mineralium Deposita* 30:246–256. <https://doi.org/10.1007/BF00196360>
- 617 Mansour A, Wagreich M, Gier S, et al (2021) Climate variability and paleoceanography during the
618 Late Cretaceous: Evidence from palynology, geochemistry and stable isotopes analyses from
619 the southern Tethys. *Cretaceous Research* 126:104831.
620 <https://doi.org/10.1016/j.cretres.2021.104831>
- 621 Martin J (1982) Le Moyen Atlas Central, étude géomorphologique. *Notes et Mémoires du Service*
622 *Géologique du Maroc* 258:445
- 623 Marzoli A, Bertrand H, Youbi N, et al (2019) The Central Atlantic magmatic province (CAMP) in
624 Morocco. *Journal of Petrology*. <https://doi.org/10.1093/petrology/egz021>
- 625 McCuaig TC, Scarselli S, O'Connor T, et al (2018) The Power of a Systems Approach to Mineral and
626 Petroleum Exploration in Sedimentary Basins. In: Arribas R. AM, Mauk JL (eds) *Metals,*
627 *Minerals, and Society*. Society of Economic Geologists (SEG), p 0
- 628 Missenard Y, Taki Z, Frizon de Lamotte D, et al (2007) Tectonic styles in the Marrakesh High Atlas
629 (Morocco): The role of heritage and mechanical stratigraphy. *Journal of African Earth*
630 *Sciences* 48:247–266. <https://doi.org/10.1016/j.jafrearsci.2007.03.007>
- 631 Missenard Y, Zeyen H, Frizon de Lamotte D, et al (2006) Crustal versus asthenospheric origin of relief
632 of the Atlas Mountains of Morocco. *Journal of Geophysical Research: Solid Earth* 111:n/a-
633 n/a. <https://doi.org/10.1029/2005JB003708>
- 634 Pouit G (1964) Les gîtes de manganèse marocains encaissés dans les Formations carbonatées :
635 éléments pour une synthèse. *Chronique des Mines et de la Recherche Minière* 371–380
- 636 Rhalmi M (1992) Les systèmes sédimentaires cénomano-turonien et sénoniens de la région
637 manganésifère d'Imini (Haut-Atlas Central, Maroc) et leur évolution diagénétique. PhD,
638 Bourgogne
- 639 Rhalmi M, Chellai EH, Michard A (2011) Mine d'Imini : manganèse stratiforme dans les couches du
640 Crétacé. In: Mouttaqi A, Rjimati EC, Maacha L, et al. (eds) *Les principales mines du Maroc,*
641 *Service géologique du Maroc. Notes et mémoires du service géologique, Rabat,* pp 75–79
- 642 Rhalmi M, Pascal A, Chellai E (2000) Lithobiostratigraphie, diagenèse et paléogéographie au
643 Cénomaniens supérieur-Turonien inférieur des bassins sud-atlasiques marocains. *Géologie*
644 *Alpine* 76:135–149
- 645 Rhalmi M, Pascal A, Lang J (1997) Contrôle sédimentaire et diagénétique de la minéralisation
646 manganésifère au cours du Crétacé Supérieur dans la région d'Imini (Haut-Atlas central,
647 Maroc). *Comptes rendus de l'Académie des sciences Série 2 Sciences de la terre et des*
648 *planètes* 323:213–220
- 649 Roddick JC, Cliff RA, Rex DC (1980) The evolution of excess argon in alpine biotites - a ^{40}Ar - ^{39}Ar
650 analysis. *Earth and Planetary Science Letters* 48:185–208. [https://doi.org/10.1016/0012-821X\(80\)90181-8](https://doi.org/10.1016/0012-821X(80)90181-8)
- 652 Ruddiman WF, Raymo ME, Prell WL, Kutzbach JE (1997) The uplift-climate connection: a synthesis.
653 In: Ruddiman WF (ed) *Tectonic Uplift and Climate Change*. Springer US, Boston, MA, pp 471–
654 515

- 655 Ruffet G, Innocent C, Michard A, et al (1996) A geochronological and study of K-Mn oxides from the
656 weathering sequence of Azul, Brazil. *Geochimica et Cosmochimica Acta* 60:2219–2232.
657 [https://doi.org/10.1016/0016-7037\(96\)00080-4](https://doi.org/10.1016/0016-7037(96)00080-4)
- 658 Thein J (1990) Paleogeography and geochemistry of the “Cenomano-Turonian” formations in the
659 manganese district of Imini (Morocco) and their relation to ore deposition. *Ore Geology*
660 *Reviews* 5:257–291. [https://doi.org/10.1016/0169-1368\(90\)90034-K](https://doi.org/10.1016/0169-1368(90)90034-K)
- 661 Thomas RJ, Fekkak A, Ennih N, et al (2004) A new lithostratigraphic framework for the Anti-Atlas
662 Orogen, Morocco. *Journal of African Earth Sciences* 39:217–226.
663 <https://doi.org/10.1016/j.jafrearsci.2004.07.046>
- 664 Turner G (1971) Argon 40-argon 39 dating: the optimization of irradiation parameters. *Earth and*
665 *Planetary Science Letters* 10:227–234. [https://doi.org/10.1016/0012-821X\(71\)90010-0](https://doi.org/10.1016/0012-821X(71)90010-0)
- 666 Vasconcelos PM (1999) K-Ar and $^{40}\text{Ar}/^{39}\text{Ar}$ geochronology of weathering processes. *Annual Review of*
667 *Earth and Planetary Sciences* 27:183–229. <https://doi.org/10.1146/annurev.earth.27.1.183>
- 668 Vasconcelos PM, Carmo I de O (2018) Calibrating denudation chronology through $^{40}\text{Ar}/^{39}\text{Ar}$
669 weathering geochronology. *Earth-Science Reviews* 179:411–435.
670 <https://doi.org/10.1016/j.earscirev.2018.01.003>
- 671 Vasconcelos PM, Renne PR, Becker TA, Wenk H-R (1995) Mechanisms and kinetics of atmospheric,
672 radiogenic, and nucleogenic argon release from cryptomelane during analysis. *Geochimica et*
673 *Cosmochimica Acta* 59:2057–2070. [https://doi.org/10.1016/0016-7037\(95\)00126-3](https://doi.org/10.1016/0016-7037(95)00126-3)
- 674 Verhaert M, Bernard A, Dekoninck A, et al (2017) Mineralogical and geochemical characterization of
675 supergene Cu–Pb–Zn–V ores in the Oriental High Atlas, Morocco. *Mineralium Deposita*.
676 <https://doi.org/10.1007/s00126-017-0753-5>
- 677 Verhaert M, Gautheron C, Dekoninck A, et al (2022) Unravelling the Temporal and Chemical
678 Evolution of a Mineralizing Fluid in Karst-Hosted Deposits: A Record from Goethite in the
679 High Atlas Foreland (Morocco). *Minerals* 12:1151. <https://doi.org/10.3390/min12091151>
- 680 Verhaert M, Madi A, Basbas AE, et al (2020) Genesis of As-Pb-Rich Supergene Mineralization: The
681 Tazalaght and Agoujgal Cu Deposits (Moroccan Anti-Atlas Copperbelt). *Economic Geology*
682 115:1725–1748. <https://doi.org/10.5382/econgeo.4779>
- 683 Wijbrans JR, McDougall I (1986) $^{40}\text{Ar}/^{39}\text{Ar}$ dating of white micas from an Alpine high-pressure
684 metamorphic belt on Naxos (Greece): the resetting of the argon isotopic system. *Contr*
685 *Mineral and Petrol* 93:187–194. <https://doi.org/10.1007/BF00371320>
- 686 York D (1968) Least squares fitting of a straight line with correlated errors. *Earth and Planetary*
687 *Science Letters* 5:320–324. [https://doi.org/10.1016/S0012-821X\(68\)80059-7](https://doi.org/10.1016/S0012-821X(68)80059-7)
- 688 York D, Evensen NM, Martínez ML, De Basabe Delgado J (2004) Unified equations for the slope,
689 intercept, and standard errors of the best straight line. *American Journal of Physics* 72:367–
690 375. <https://doi.org/10.1119/1.1632486>
- 691 Zammit R, Lear CH, Samankassou E, et al (2022) Early Miocene Intensification of the North African
692 Hydrological Cycle: Multi-Proxy Evidence From the Shelf Carbonates of Malta.
693 *Paleoceanography and Paleoclimatology* 37:e2022PA004414.
694 <https://doi.org/10.1029/2022PA004414>

695 Zouhri S, Kchikach A, Saddiqi O, et al (2008) The Cretaceous-Tertiary Plateaus. In: Michard A, Saddiqi
696 O, Chalouan A, Lamotte DF de (eds) Continental Evolution: The Geology of Morocco.
697 Springer Berlin Heidelberg, Berlin, Heidelberg, pp 331–358

698

699

700 **Figure caption**

701 **Fig. 1** Geological map of the Moroccan High Atlas and its southern foreland (modified after Leprêtre et al.,
702 2018), with location of samples and the Imini and Tasdremt Mn districts (see Fig. 2a for sampling in the Imini
703 district). NAF: North Atlas Front; MF: Medinet Fault; TTFZ: Tizin'Test Fault Zone; SAF: South Atlas Front;
704 OkT: Oukaimeden Thrust; SFT: Sidi Fars Thrust; AAMF: Anti-Atlas Major Fault; Azg.: Azegour.

705 **Fig. 2 a** Geological map of the Imini foreland showing the extension of the Mn deposits and the location of the
706 sampling sites (modified after Leprêtre et al. (2015)). **b** Stratigraphic section of the Cenomanian-Turonian (CT)
707 dolostone at Lantenois showing the three Mn orebodies (modified after Gutzmer et al., 2006). **c** Schematic cross-
708 section of the South Atlasic Front and the Imini foreland showing the general pinch out of Jurassic and Triassic
709 rocks and open folds of the Cenozoic cover (modified after Missenard et al. (2007), Zouhri et al. (2008), Leprêtre
710 et al. (2015).

711 **Fig. 3 a** Vertical C2 and C3 ore at Timkit near the Imini fold. **b** C1 Mn ore with stockwork mineralization in the
712 Bou Aguioun pit. **c** Offset of the CT level at Lantenois. A decametric flexure corresponds to the southern limit of
713 the mineralization. Barren CT dolostone is observed south when it is mineralized north. **d** C2 and C3 Mn ore at
714 Lantenois. **e** C3 Mn ore in the Far West area.

715 **Fig. 4** Paragenetic sequence of the mineralization in the Imini district (modified from Dekoninck et al. 2016a;
716 Verhaert et al. 2022). Ho=hollandite, Cry=cryptomelane, Co=coronadite.

717 **Fig. 5** Petrographic features of Mn oxide samples. **a** Colloform cryptomelane (stage 2) of C3 ore growing on the
718 dolomite (stage 1) at Lantenois. **b** Colloform cryptomelane (stage 2) of C1 ore growing on dolomite (stage 1) at
719 Bou Aguioun. Late calcite veins (Ca) contains reworked dolomite (Do), quartz, feldspar and cryptomelane grains.
720 **c** Brecciated hollandite stage 2 growing on colloform goethite fragment in C3 ore. **d** Pyrolusite laths (stage 2)
721 growing on stage 1 hollandite with dolomite rhomb remnants at Bou Aguioun (C2 ore).

722 **Fig. 6** $^{40}\text{Ar}/^{39}\text{Ar}$ data of the Priabonian Mn phase. **a**. Density probability diagram of resized (De Putter and Ruffet
723 2020) apparent ages. **b-e** Age and $^{37}\text{Ar}_{\text{Ca}}/^{39}\text{Ar}_{\text{K}}$ spectra ($^{37}\text{Ar}_{\text{Ca}} \# \text{Ca}$ and $^{39}\text{Ar}_{\text{K}} \# \text{K}$ with $^{37}\text{Ar}_{\text{Ca}}/^{39}\text{Ar}_{\text{K}} =$
724 $\text{CaO}/\text{K}_2\text{O}/2.179$; Deckart et al., 1997). PA and PPA ages assumed to be valid are shown in bold. Unvalidated ages
725 are shown in grey. Apparent age error bars are at the 1σ level; errors in the J-parameter are not included. PA and
726 PPA ages (1σ uncertainties including errors in the J-parameter) are given where applicable. Inverse isochron
727 diagrams ($^{36}\text{Ar}_{\text{atm}}/^{40}\text{Ar}_{\text{atm}}$ vs. $^{39}\text{Ar}_{\text{K}}/^{40}\text{Ar}^*$) with least squares fitting of the best straight line according to York

728 (1968) and York et al. (2004). Grey ellipses are excluded from isochron regression. Unvalidated data are shown
729 in as grey stars. The mean age of the event is the weighted mean of the validated plateau (PA) and pseudo-plateau
730 (PPA) ages. Detailed data is in ESM S3.

731 **Fig. 7** $^{40}\text{Ar}/^{39}\text{Ar}$ data of the Miocene Mn phase. **a.** Density probability diagram of resized (De Putter and Ruffet
732 2020) apparent ages. **b-h.** Age and $^{37}\text{Ar}_{\text{Ca}}/^{39}\text{Ar}_{\text{K}}$ spectra. Degassing diagram of samples IM98-EX and 18TIF02
733 presenting $(^{39}\text{Ar}_{\text{K}}/\Delta V_{\text{T}^\circ}) / (^{39}\text{Ar}_{\text{K}}/\Delta V_{\text{T}^\circ})_{\text{Max}}$ vs. $\%^{39}\text{Ar}_{\text{K}}$ (see text for explanation). $\Delta V_{\text{T}^\circ}$ corresponds to the laser
734 power control voltage increment. Weighted age spectrum of sample 18TIF02. Refer to Fig. 6 for explanations.

735 **Fig. 8** $^{40}\text{Ar}/^{39}\text{Ar}$ data of the Cretaceous to late Paleocene Mn phase. **a.** Density probability diagram of resized (De
736 Putter and Ruffet 2020) apparent ages. **b-h.** Age and $^{37}\text{Ar}_{\text{Ca}}/^{39}\text{Ar}_{\text{K}}$ spectra. Refer to Figs. 6 and 7 for explanations.

737 **Fig. 9** Pb isotopic ratios of the Imini and Tasdremt Mn ore samples and potential source rocks. **a-b** Recalculated
738 $(^{206}\text{Pb}/^{204}\text{Pb})_{\text{in}}$ vs. $(^{207}\text{Pb}/^{204}\text{Pb})_{\text{in}}$ at 67 Ma. Lead isotopic data for the Jurassic carbonates and sandstones are from
739 Bouabdellah et al. (2015). Neoproterozoic Pb isotopic values of galena are from Bouabdellah et al. (2016), and
740 those of MVT deposits are from Bouabdellah et al. (2012, 2015). Galena Pb isotopic values are not recalculated.
741 The 67 Ma recalculated values from Triassic basalts are complemented by data of Marzoli et al. (2019). All the
742 Pb isotopic data were obtained on unleached whole rocks, except for the Triassic basalts. **c** Pb isotope ratios of
743 unleached and leached basalts.

744 **Fig. 10** Time-event chart of the Imini Mn ore deposits illustrating the multistage Mn deposition based on $^{40}\text{Ar}/^{39}\text{Ar}$
745 geochronological data and of Dekoninck et al. (2021) (Tasdremt area). Sedimentation pulses in the CT and late
746 Santonian stages at Imini are from Rhalmi et al. (2000, 1997) and Algouti et al. (1999). The Paleocene to late
747 Eocene and late Miocene pulses of the western Ouarzazate basin are from El Harfi et al. (2001) and Leprêtre et
748 al. (2015). Early Atlasic doming (D0) and Cenozoic Atlasic uplift (D1-3) are from Leprêtre et al. (2018) and
749 Leprêtre et al. (2015), respectively. Fe mineralization events are from Verhaert et al. (2022).

750 **Fig. 11** Metallogenic sketch illustrating the multistage formation of the Imini Mn oxide deposits and their
751 relationships to uplift events in the Atlas belt. Geodynamic phases are from Leprêtre et al. (2015, 2018). Mn
752 transport and deposition setting are from Gutzmer et al. (2006).

753

754 **Table caption**

755 **Table 1** Summary of significant geochronological data and validated ages (Plateau (PA) and Pseudo-Plateau
756 (PPA) ages and Isochron ages based on $^{40}\text{Ar}/^{39}\text{Ar}$ and $^{37}\text{Ar}_{\text{Ca}}/^{39}\text{Ar}_{\text{K}}$ spectra and Inverse isochron (correlation)
757 diagrams ($^{36}\text{Ar}_{\text{atm}}/^{40}\text{Ar}_{\text{atm}}$ vs. $^{39}\text{Ar}_{\text{K}}/^{40}\text{Ar}^*$) of coronadite group minerals in the Imini district. Plateau ages are
758 shown in bold type. $(^{36}\text{Ar}/^{40}\text{Ar})_i$ is the y-axis intercept of the best straight line using the least squares method
759 developed by York (1968) and York et al. (2004). Refer to the text for discussion.

760 **Appendix A. Supplementary Material**

761 **ESM S1.** Details of the $^{40}\text{Ar}/^{39}\text{Ar}$ and Pb isotope analytical procedures.

762 **ESM S2.** Lead, uranium, and thorium abundances and lead isotope compositions of the Tasdremt-Imini Mn ores
763 and of potential metal source rocks of from Neoproterozoic to late Cretaceous. AA=Anti-Atlas; S=Siroua; S-
764 MHA= Southern Marrakech High Atlas; M-MHA= Middle Marrakech High Atlas; MA= Middle Atlas. Initial
765 ages of Neoproterozoic volcanic rocks are from Gasquet et al. (2005), Neoproterozoic Mn ores are from Lippolt
766 and Hautmann (1995), Cambrian basalts are from Landing et al. (1998), Ordovician shales are from Cornée and
767 Destombes (1991), Triassic basalts are from Marzoli et al. (2019), Triassic red sandstones are from El Arabi et al.
768 (2006), CT dolostones are from Rhalmi et al. (2000, 1997), Senonian sediments are from Algouti et al. (1999),
769 Tasdremt Mn ores are from Dekoninck et al. (2021).

770 **ESM S3.** Analytical data and parameters used for calculations of $^{40}\text{Ar}/^{39}\text{Ar}$ results. Pure K, Ca, and Cl salts; mass
771 discrimination; atmospheric argon ratios; J-parameter; and decay constants.

772 **ESM S4.** Major and trace element geochemistry.

773 **ESM S5.** K-Ar ages of coronadite group minerals in the Imini deposits. No ages are relevant for this study given
774 the complexity of the Ar/Ar spectra.

775 **ESM S6.** $^{208}\text{Pb}/^{204}\text{Pb}$ vs $^{207}\text{Pb}/^{204}\text{Pb}$ and $^{208}\text{Pb}/^{204}\text{Pb}$ vs $^{206}\text{Pb}/^{204}\text{Pb}$ plots of the Imini and Tasdremt Mn ores and
776 potential source rocks.

777 **ESM S7.** Altered basalts in the Atlas range. **a** Microscopic view of blue chayesite $[\text{K}(\text{Mg},\text{Fe}^{2+})_4\text{Fe}^{3+}\text{Si}_{12}\text{O}_{30}]$ under
778 polarized light in Triassic basalt at Telouet (Figs. 1b and 2a). **b** Microscopic view of silicified Triassic basalt with
779 chlorite-quartz druses under polarized light at Toufliht (Fig. 1b).

Table 1

Intraplate orogenesis as a driver of multistage karst-hosted mineralization: the Imini manganese case

Augustin DEKONINCK^{(1,2)@}, Jocelyn BARBARAND⁽³⁾, Gilles RUFFET^(4,5), Yves MISSEARD⁽³⁾, Nadine MATT

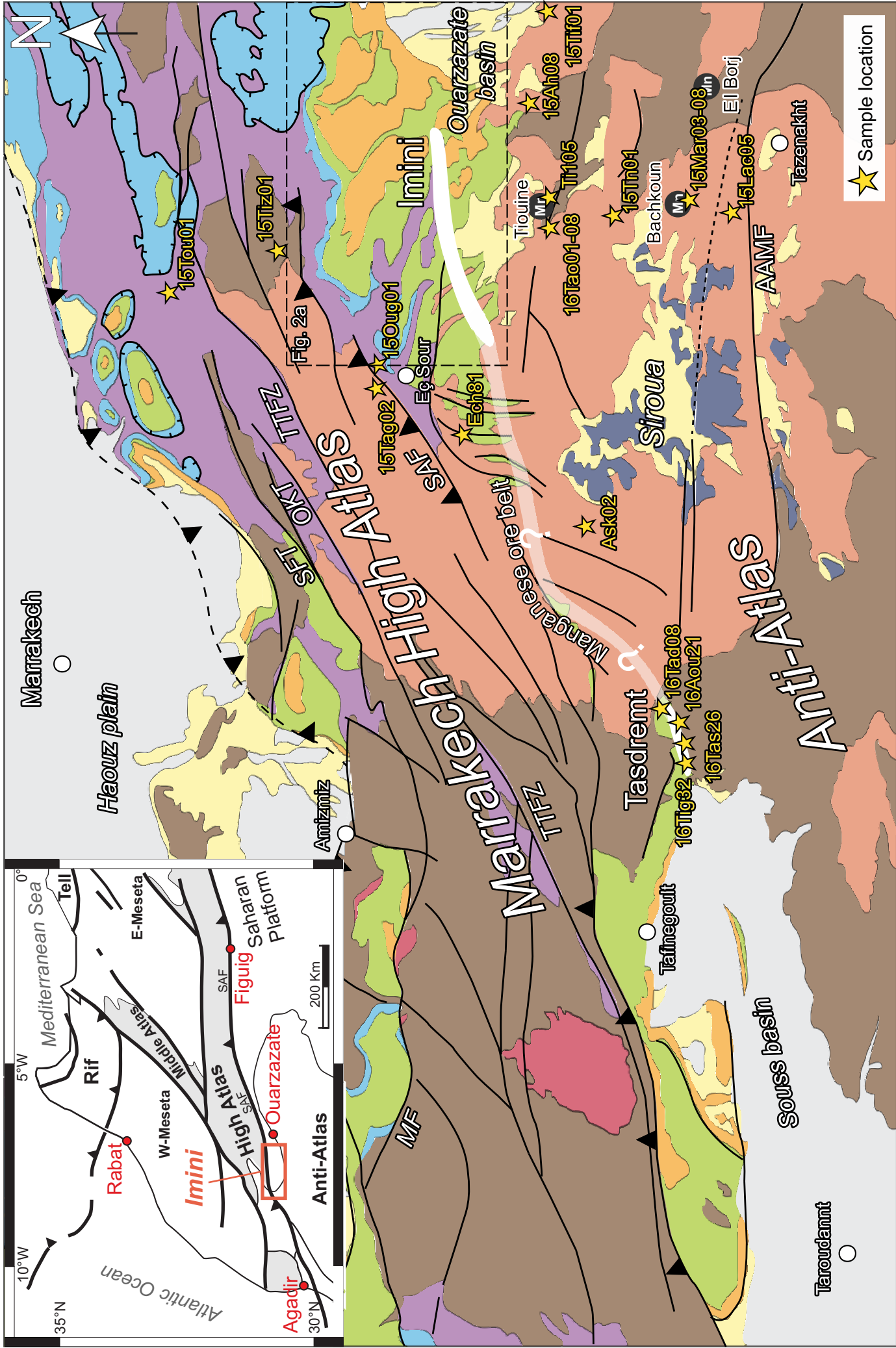
Label	Location	Ore body	PA (*) or PPA (Ma)	±1σ	Isochron age (Ma)	±1σ	(⁴⁰ Ar/ ³⁶ Ar) _i	±1σ
IM98-C	Bou Aguioun	C ₁	19.7*	0.1	19.6	0.1	313.1	7.6
IM98-EX	Bou Aguioun	C ₁	-	-	-	-	-	-
ECH102b	Bou Aguioun	C ₁	19.8*	0.1	19.8	0.1	339.9	47.2
ECH104	Bou Aguioun	C ₁	19.8*	0.1	19.5	0.3	473.9	177.7
IM36	Timkit	C ₁ -C ₂	66.6	0.2	67.0	1.0	158.8	308.4
IM40	Timkit	C ₁ -C ₂	-	-	-	-	-	-
IM37	Timkit	C ₁ -C ₂	-	-	-	-	-	-
IM39	Timkit	C ₁ -C ₂	-	-	-	-	-	-
18BA01	Bou Aguioun	C ₂	-	-	-	-	-	-
IM41d	Far West	C ₃	61.8	0.3	61.4	1.4	316.5	60.6
LAN57	Lantenois	C ₃	61.6	0.3	61.0	0.8	303.1	6.2
LAN18	Lantenois	C ₃	-	-	-	-	-	-
LAN59	Lantenois	C ₃	-	-	-	-	-	-
18PL12b	Plateau	C ₃	36.8	0.6	36.5	1.3	300.5	6.3
18TIF02	Tiffersine	C ₃	13.0	0.3	12.9	0.3	299.7	2.2
18TIF02	Tiffersine	C ₃	-	-	-	-	-	-
18TIF13	Tiffersine	C ₃	13.1	0.3	13.0	1.2	297.7	2.7
18TIF03	Tiffersine	C ₃	35.6	1.8	36.3	3.0	298.0	1.9
18TIF03	Tiffersine	C ₃	-	-	-	-	-	-
18TIF05	Tiffersine	C ₃	36.3*	1.1	36.0	1.7	298.8	1.3
18TIF12	Tiffersine	C ₃	35.5	0.9	36.0	1.9	297.9	2.2
ECH101b 4 exp.	Bou Aguioun	Stockwork	20.1*	0.1	19.9	0.1	343.7	7.6
ECH103	Bou Aguioun	Stockwork	19.1*	0.1	19.2	0.1	291.4	15.8

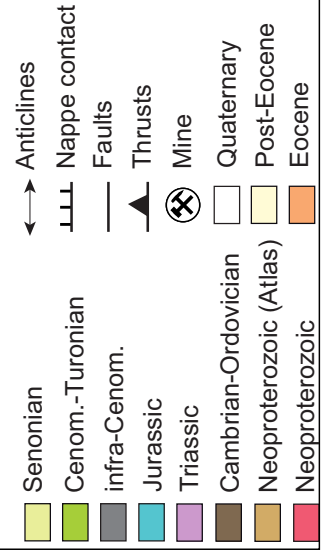
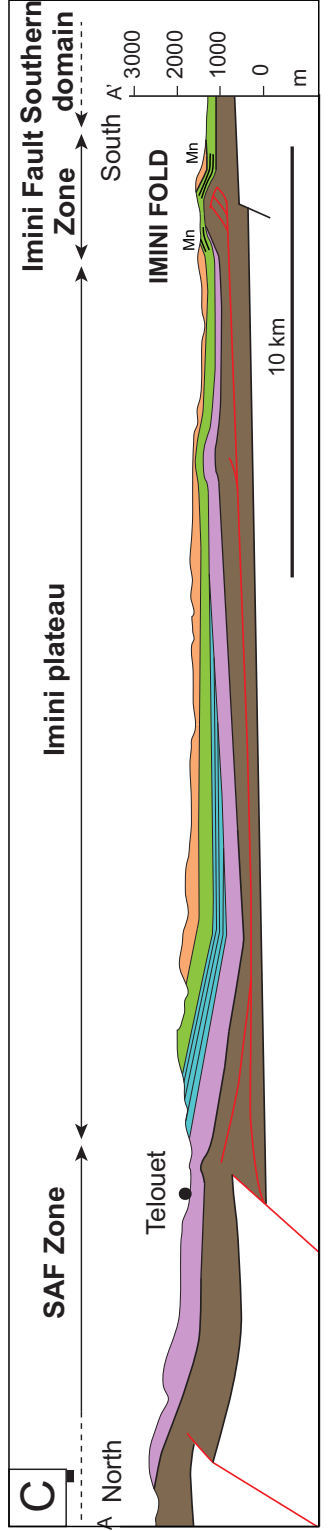
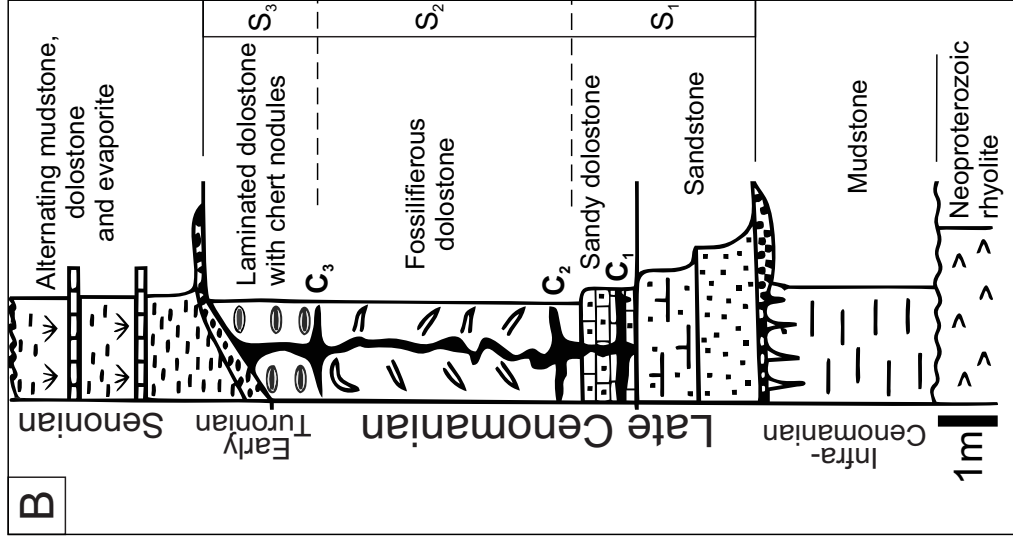
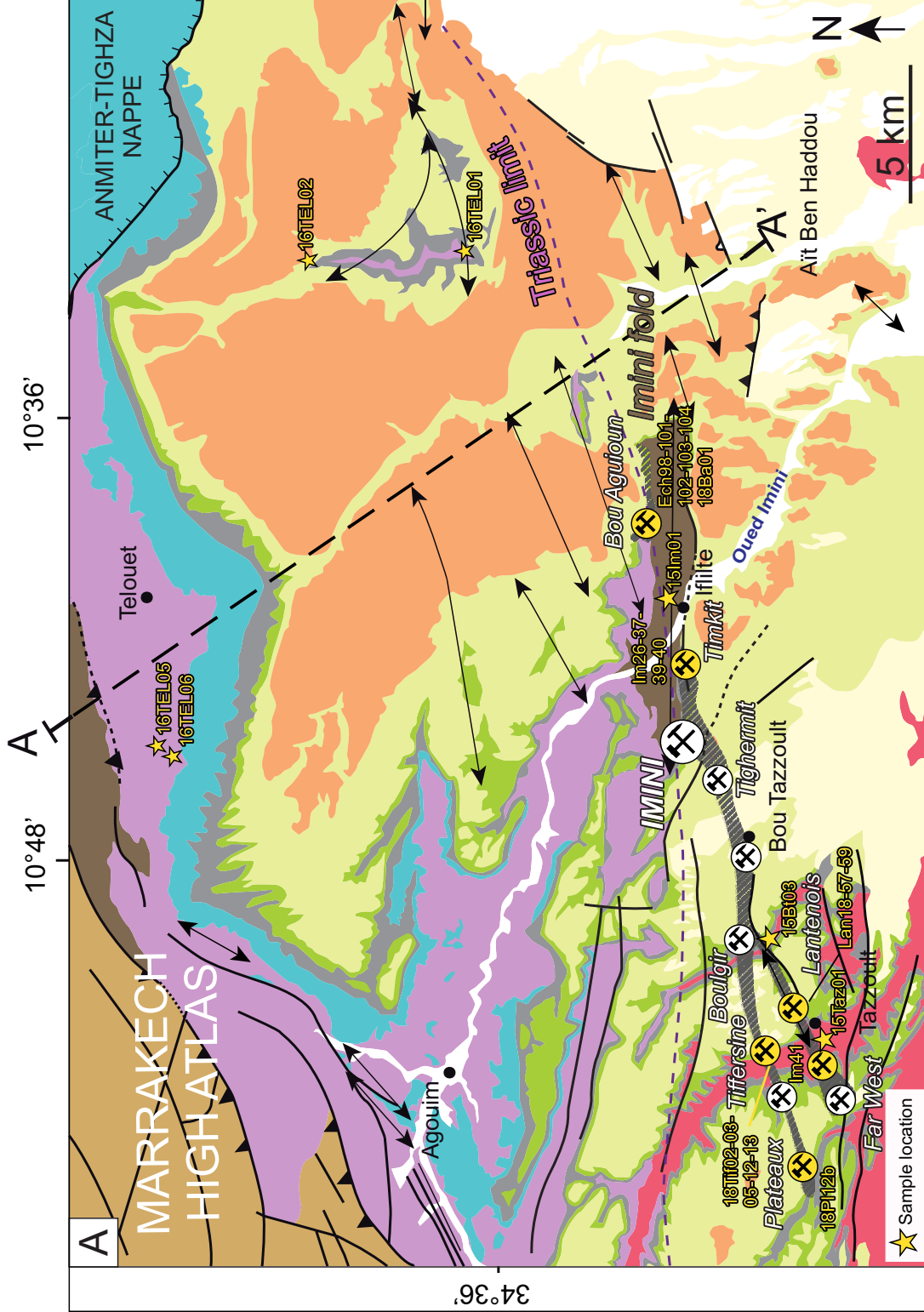
(Atlas, Morocco)

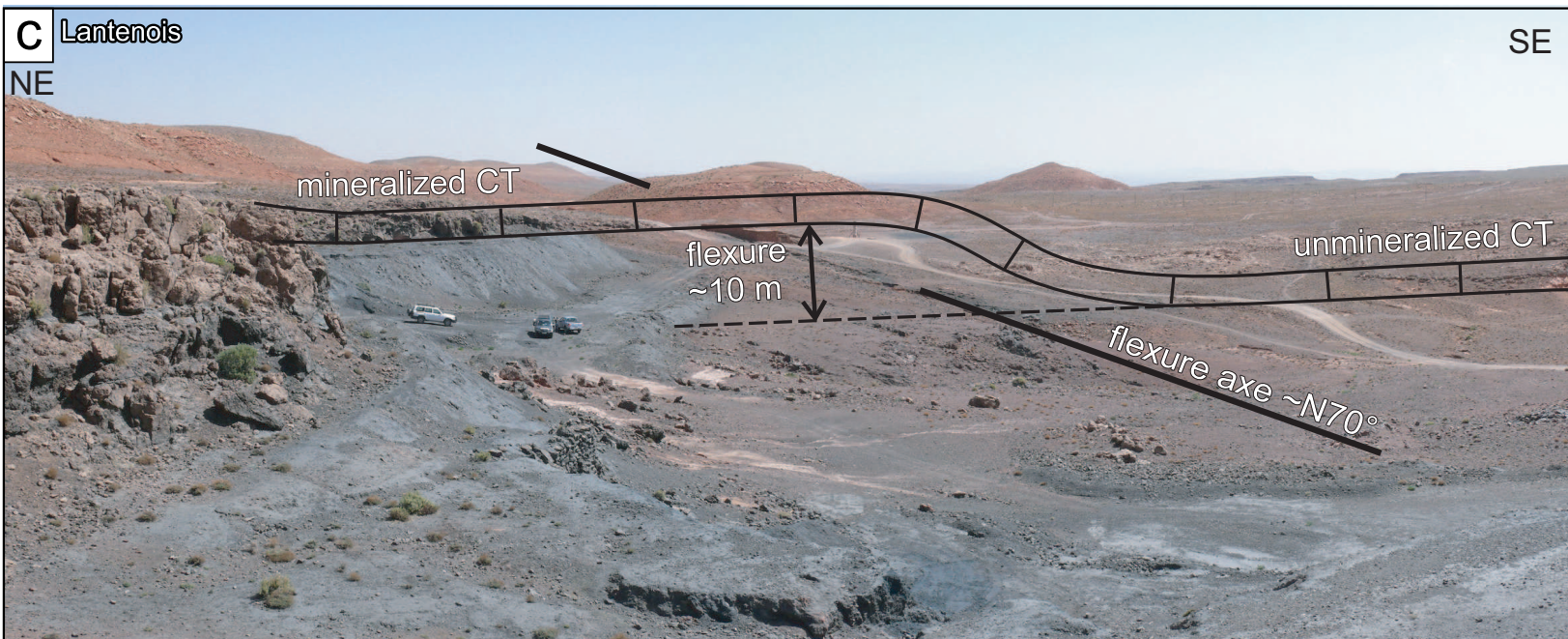
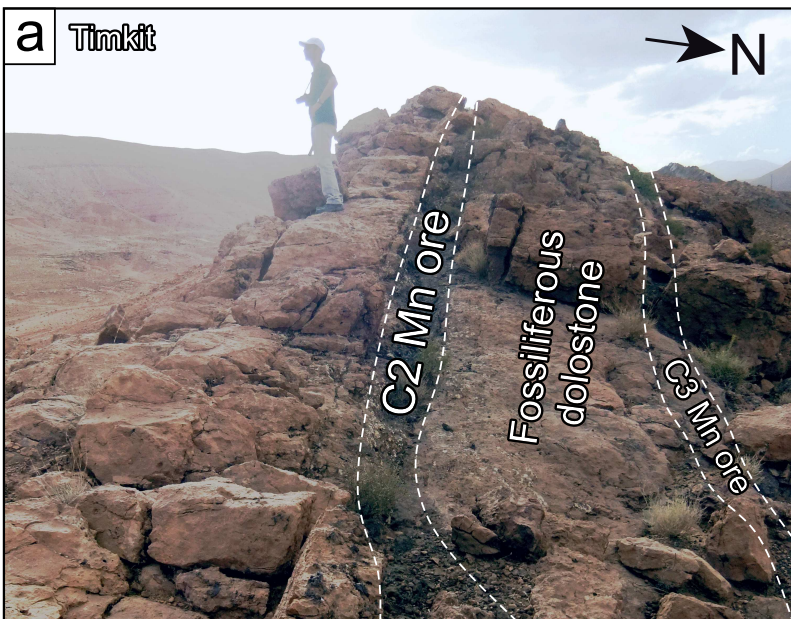
TELLI⁽²⁾, Rémi LEPRETRE^(3,6), Abdellah MOUTTAQI⁽⁷⁾, Michèle VERHAERT⁽¹⁾, Omar SADDIQI⁽⁸⁾, Johar

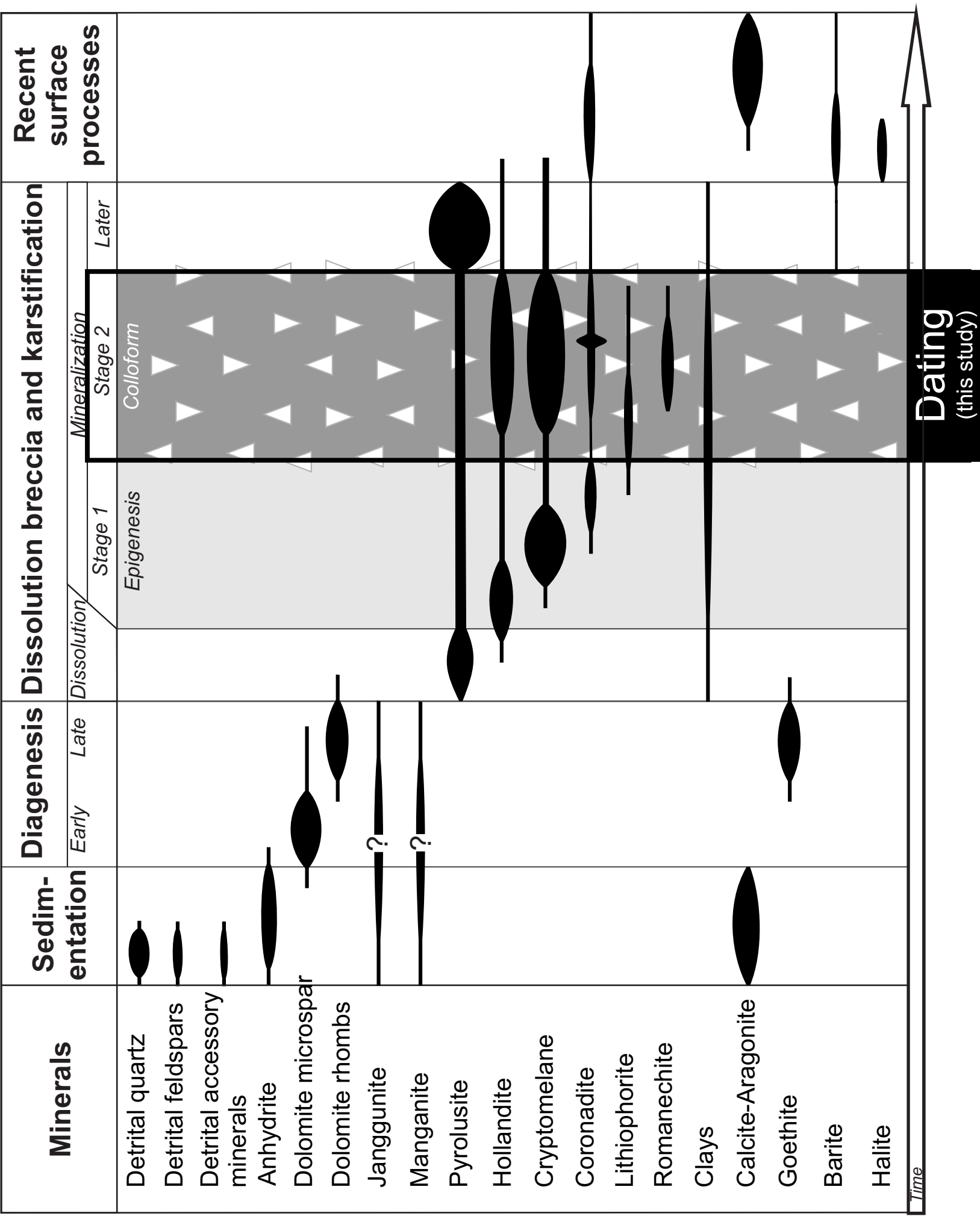
Oldest radiogenic component	Youngest radiogenic component	Comments
		Plateau
		Hump
		Plateau
		Plateau
Maastrichtian #Phase 3 Tasdremt	Paleocene & Priabonian/Miocene	Staircase
Maastrichtian #Phase 3 Tasdremt	Paleocene	Hump
not identified	not identified	Saddle
not identified	not identified	Saddle
Campanian #Phase 2 Tasdremt	Paleocene	Staircase
Campanian #Phase 2 Tasdremt	Paleocene	Staircase
Campanian #Phase 2 Tasdremt	Paleocene	Staircase
Campanian #Phase 2 Tasdremt	Paleocene	Staircase
Campanian #Phase 2 Tasdremt	Paleocene	Staircase
Priabonian	Miocene	Staircase - Ca-rich
Priabonian	Miocene	Staircase
		Irregular
Priabonian	Miocene	Staircase
≥ Paleocene	Priabonian	Staircase - Ca-rich
Priabonian	Miocene	Staircase - Ca-rich
		Plateau - Ca-rich
≥ Paleocene	Priabonian	Staircase - Ca-rich
Miocene (19.3-20.5 Ma)		Plateau
		Plateau

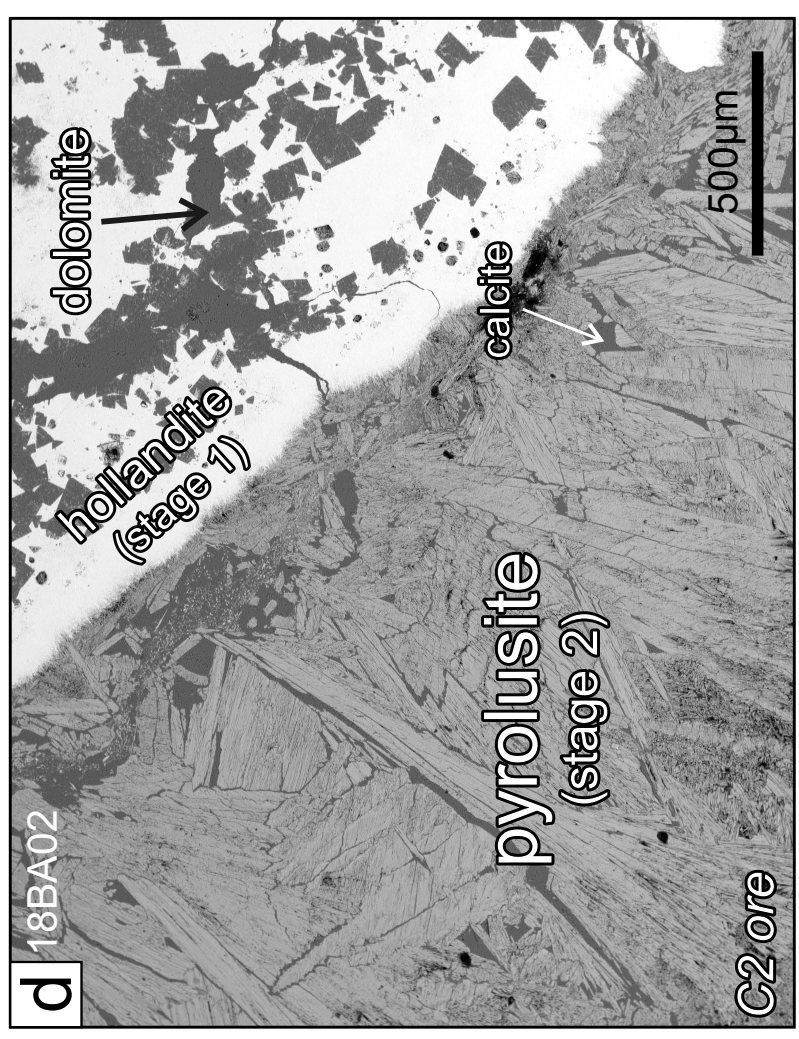
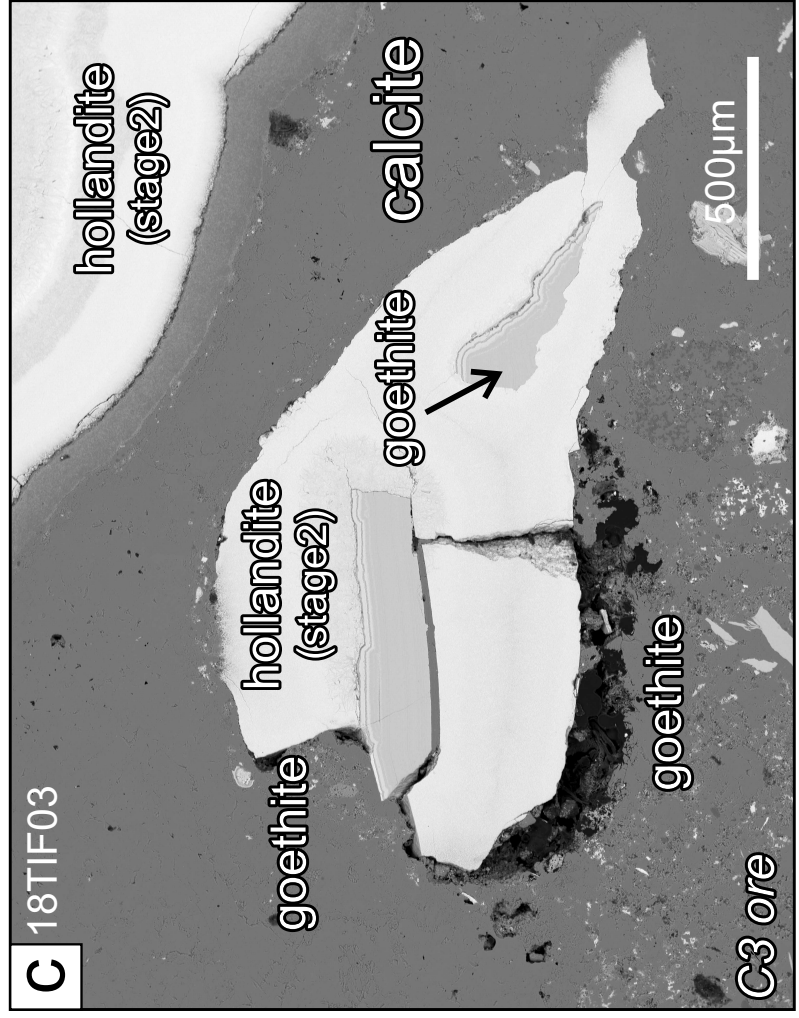
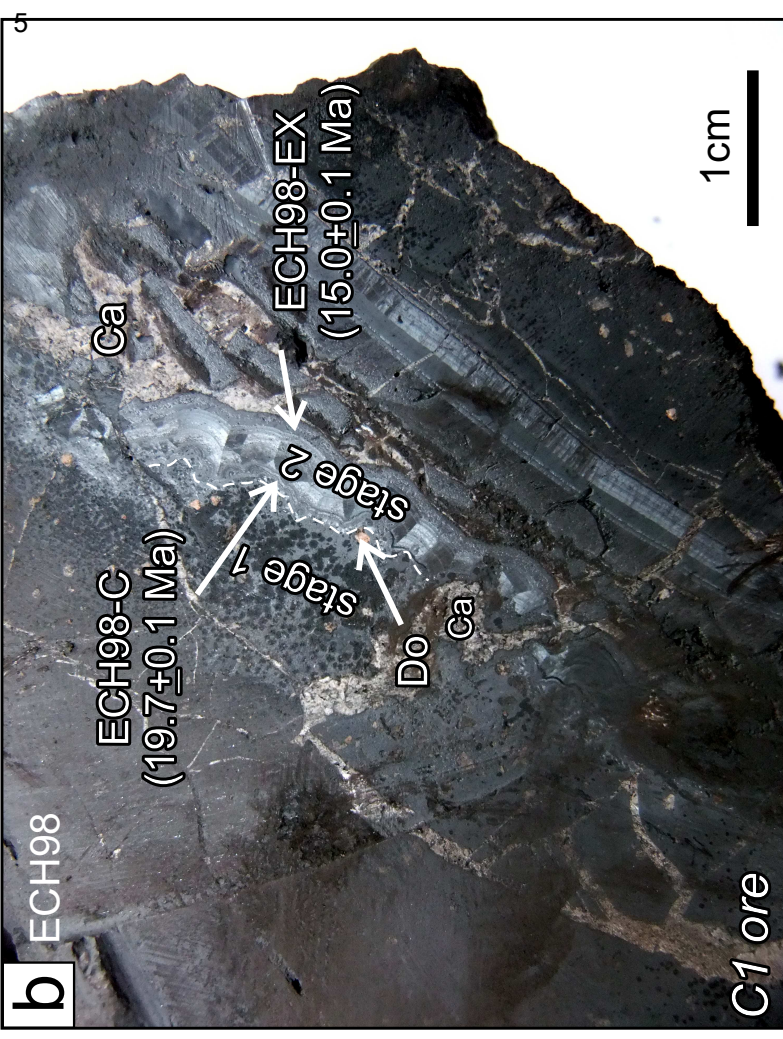
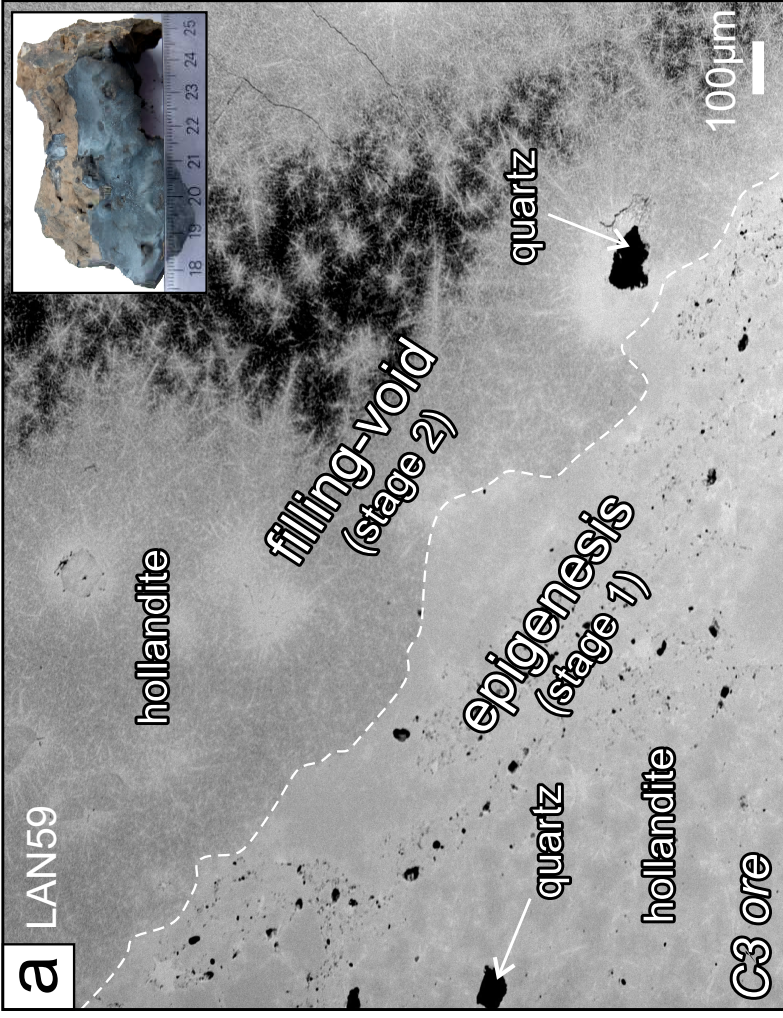
YANS⁽¹⁾

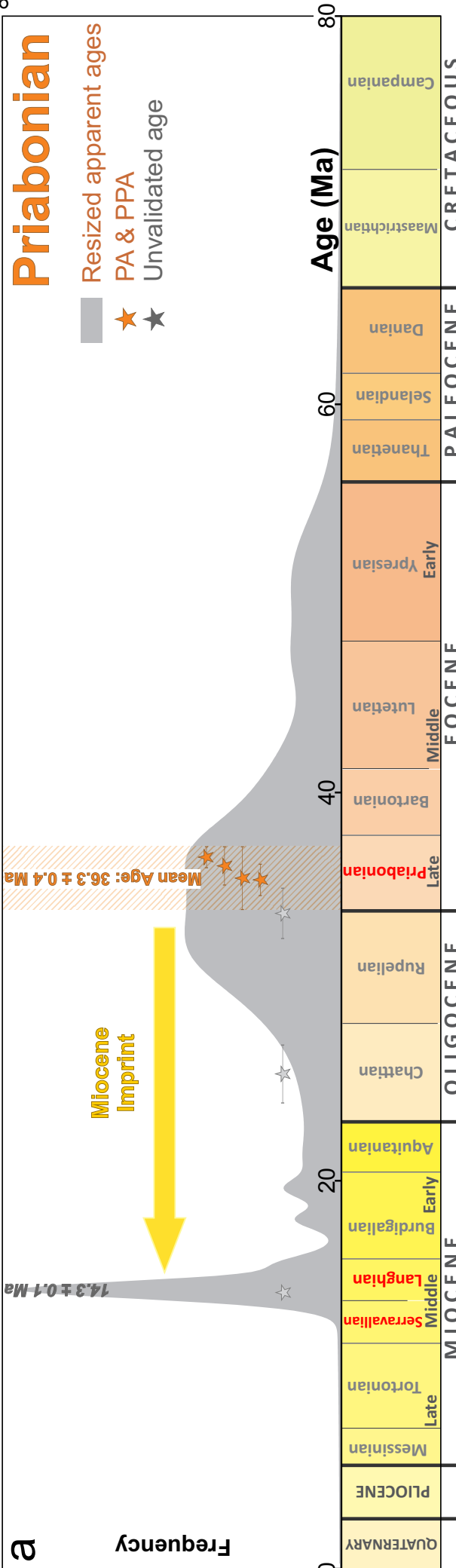




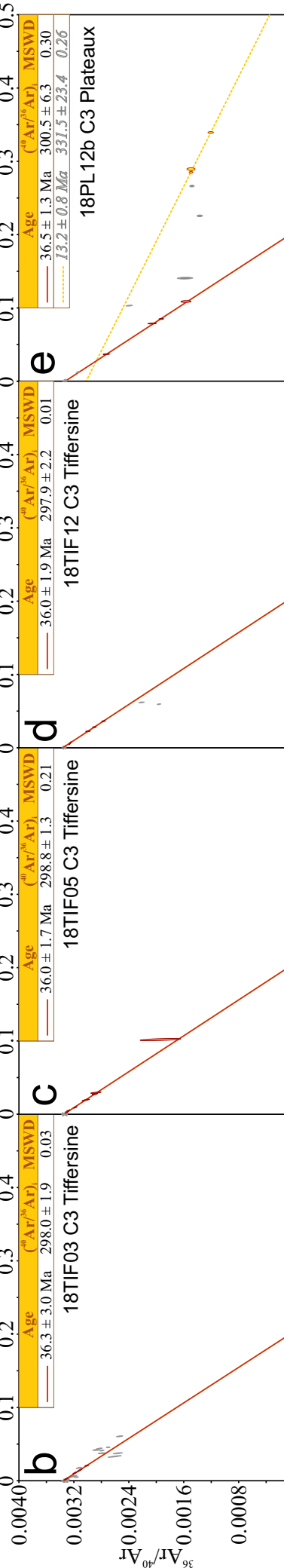
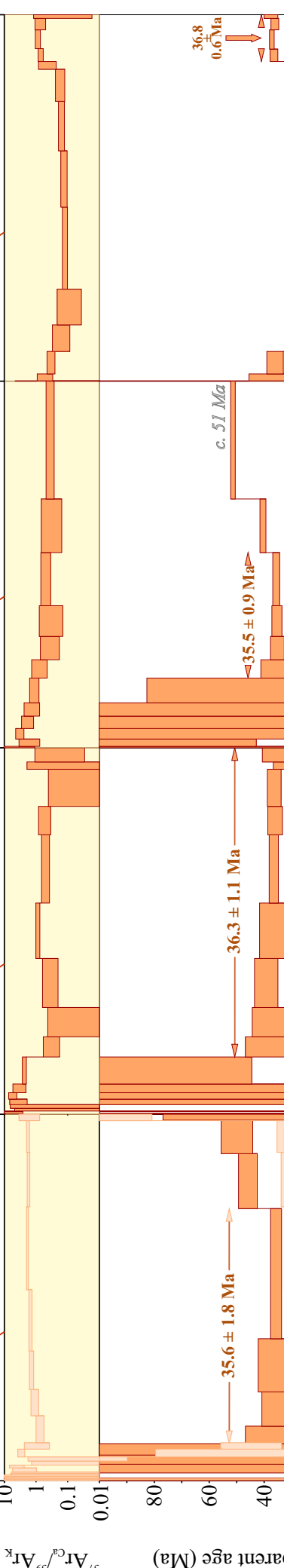
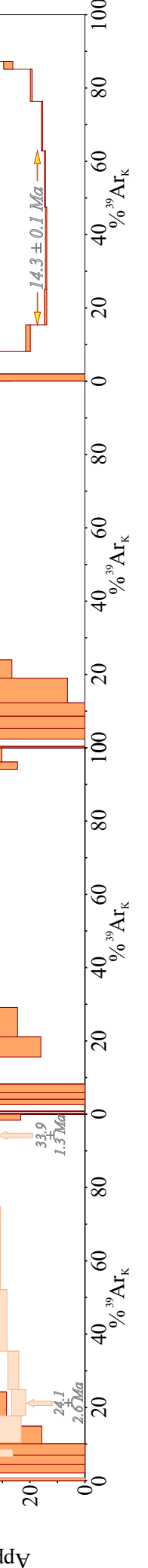
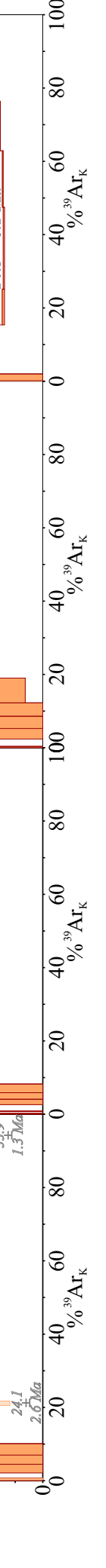






a

- Resized apparent ages
- ★ PA & PPA
- ★ Unvalidated age

b**c****d****e**

Apparent age (Ma)

 $^{37}\text{Ar}/^{39}\text{Ar}$ $^{36}\text{Ar}/^{40}\text{Ar}$ $^{39}\text{Ar}/^{40}\text{Ar}$ $^{39}\text{Ar}/^{40}\text{Ar}_k$ $^{39}\text{Ar}/^{40}\text{Ar}_k$

36.8 Ma

0.6 Ma

14.3 ± 0.1 Ma

35.5 ± 0.9 Ma

36.3 ± 1.1 Ma

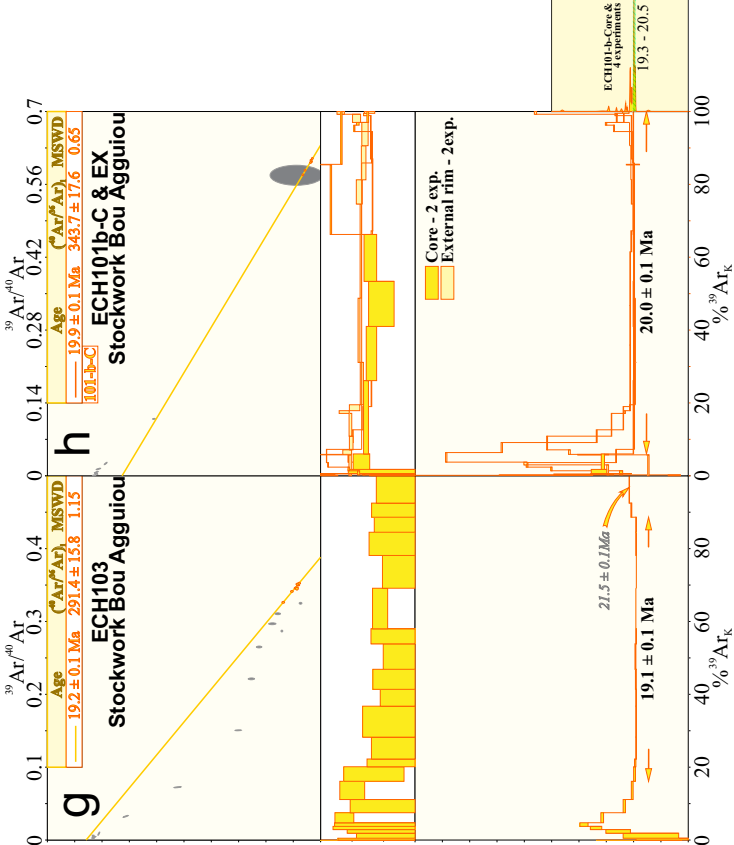
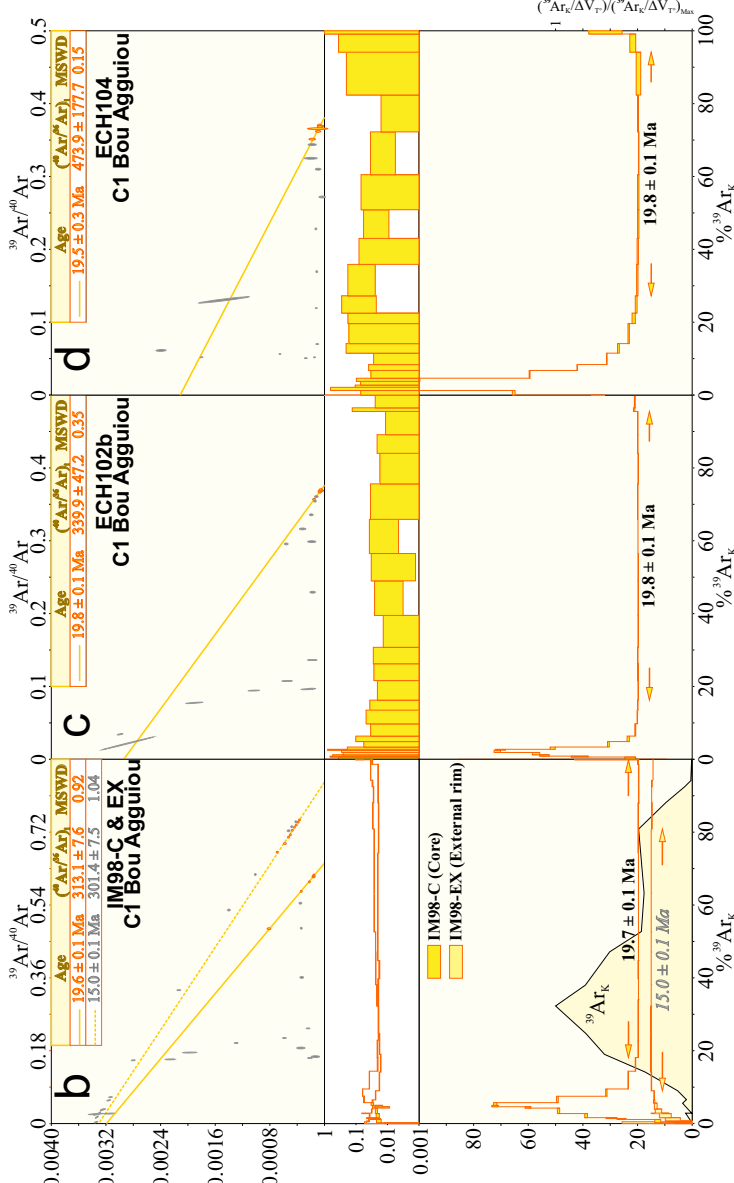
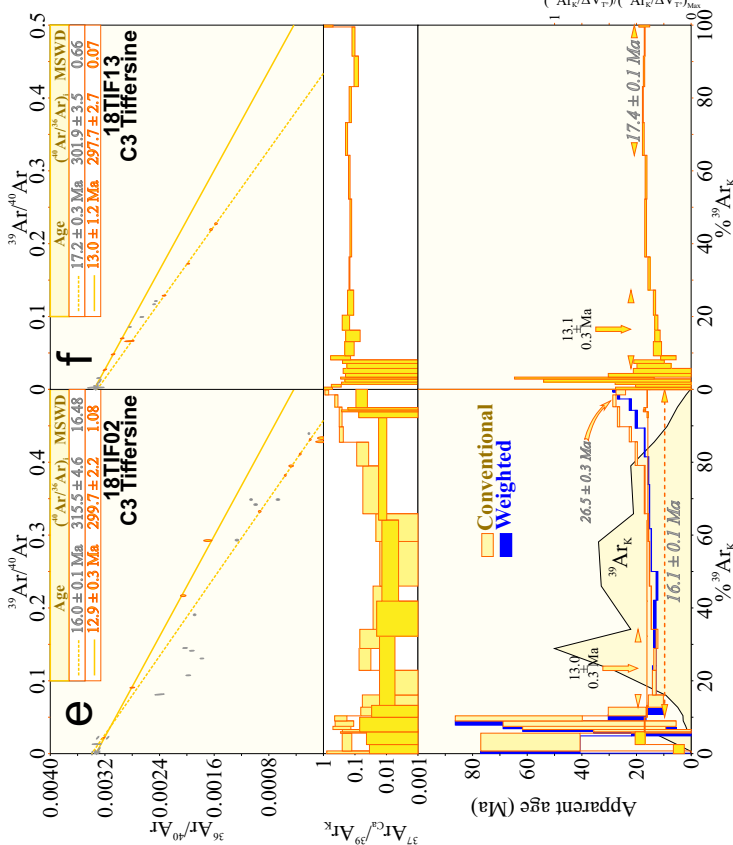
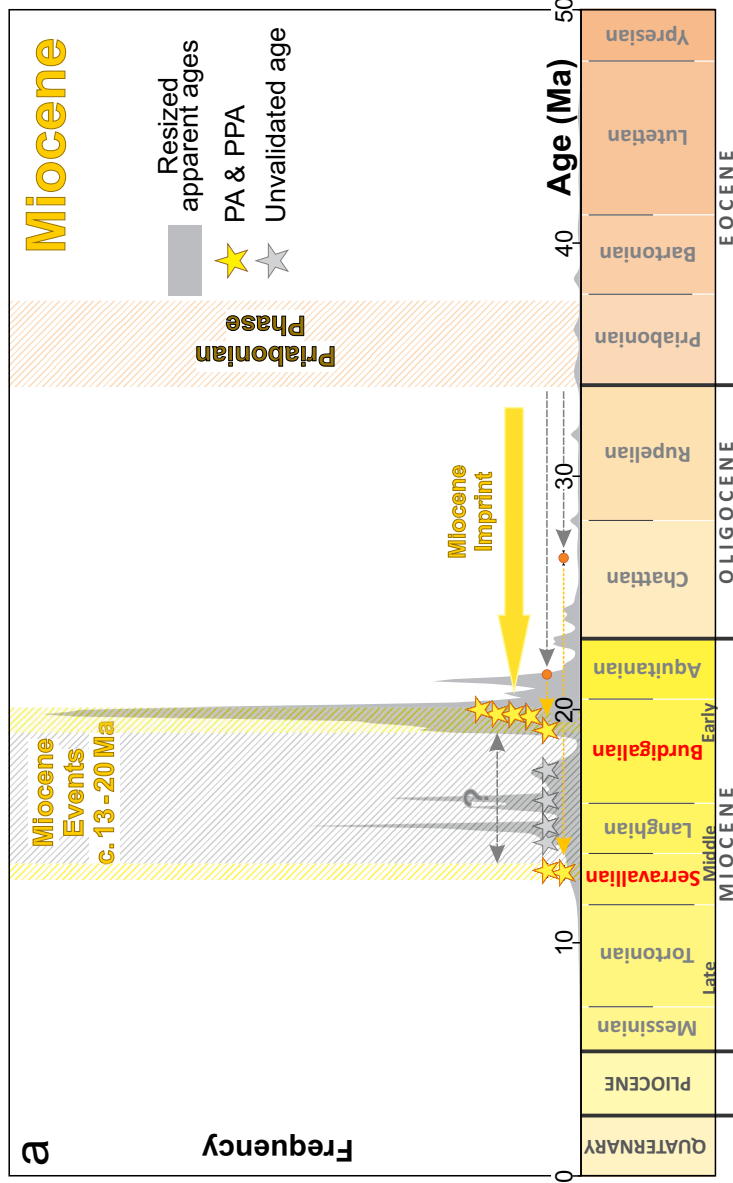
33.9 Ma

1.3 Ma

24.1 Ma

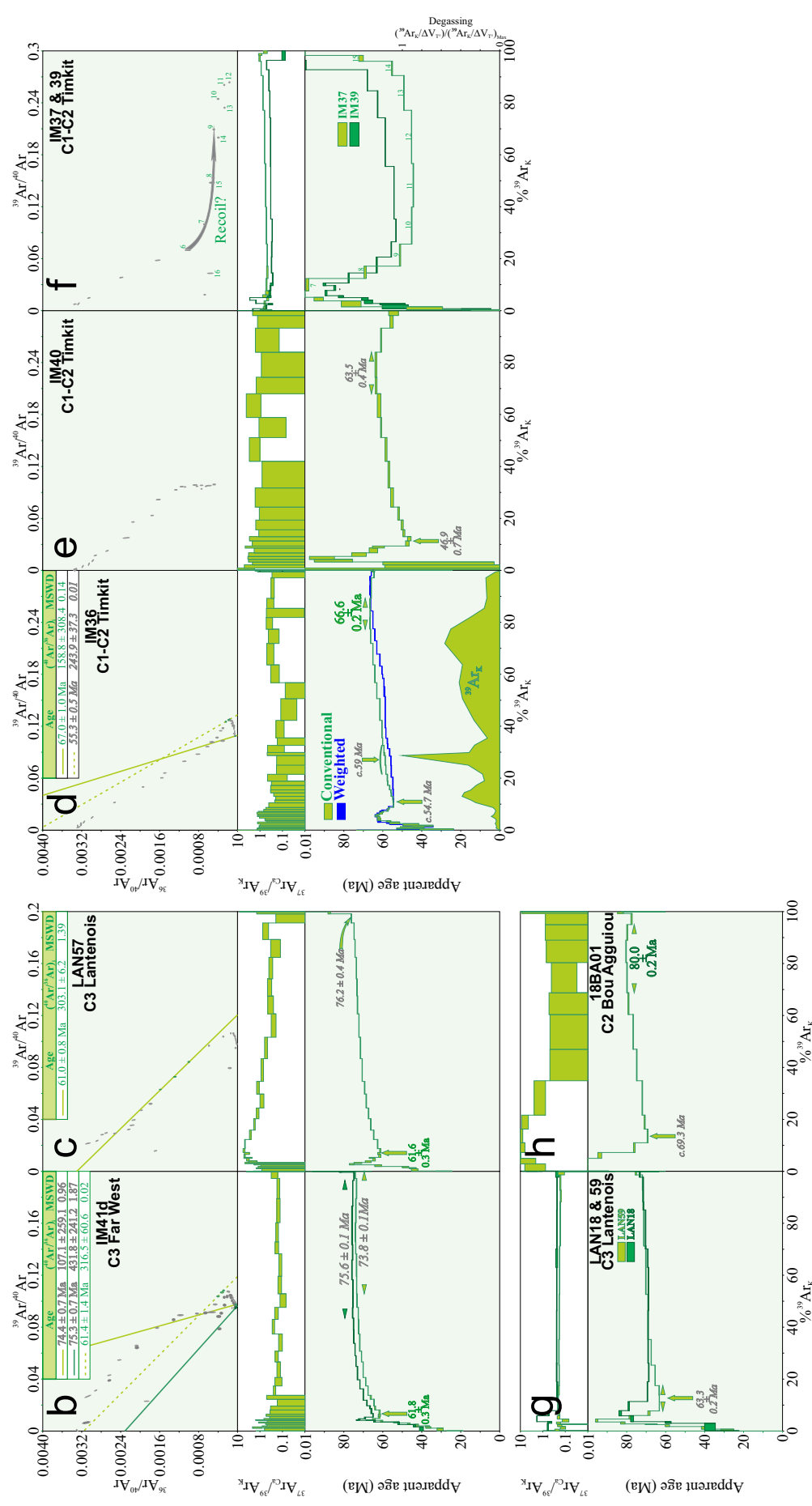
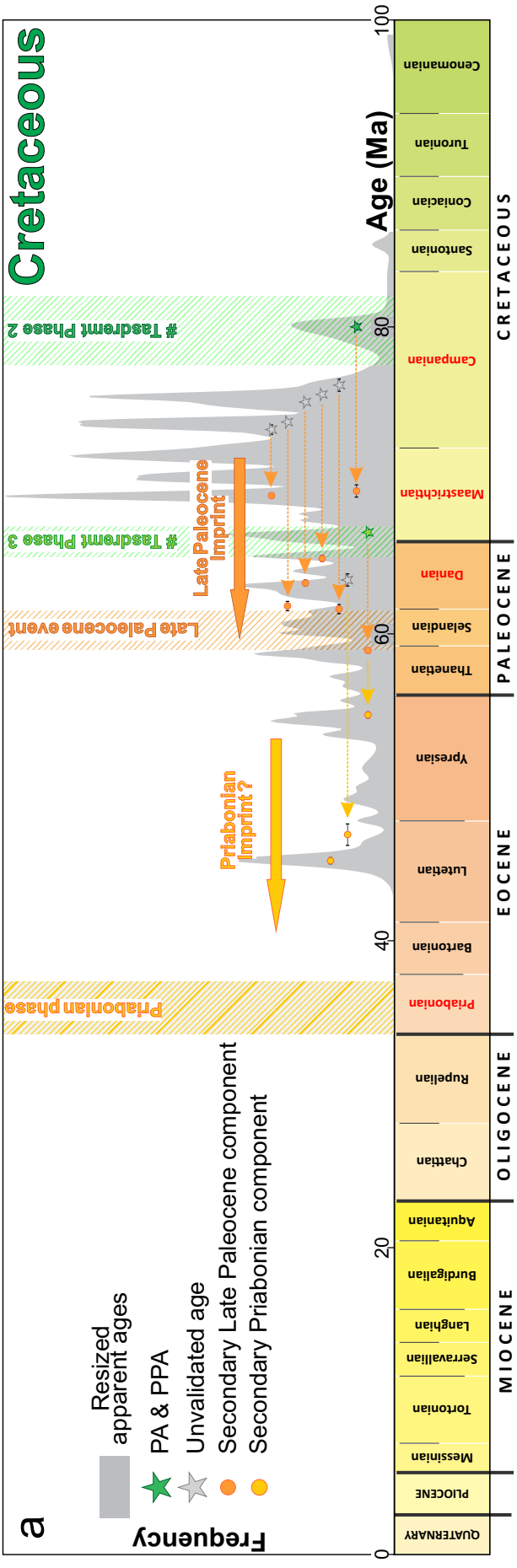
2.6 Ma

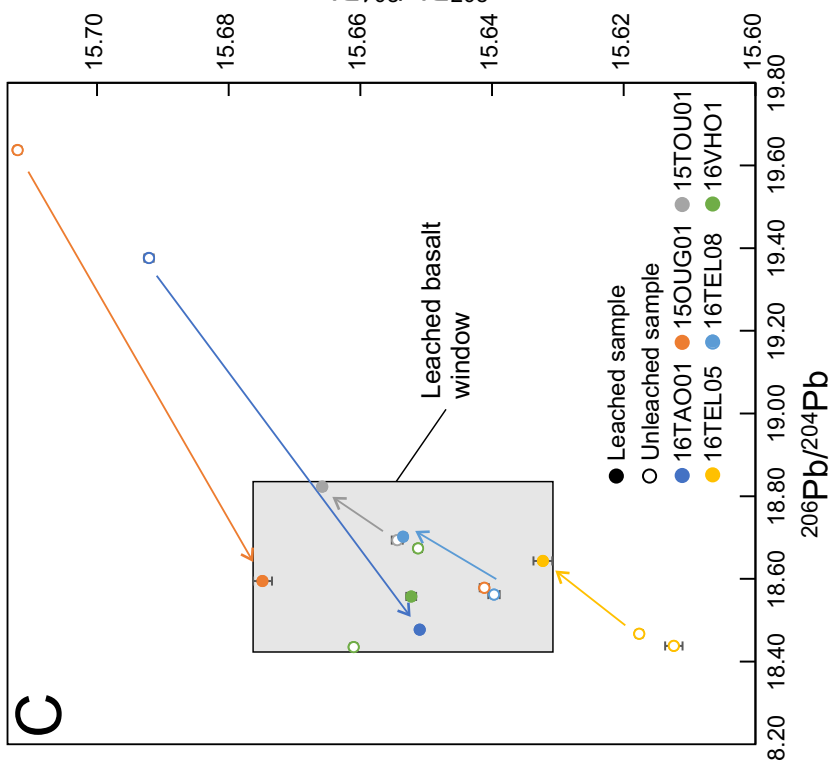
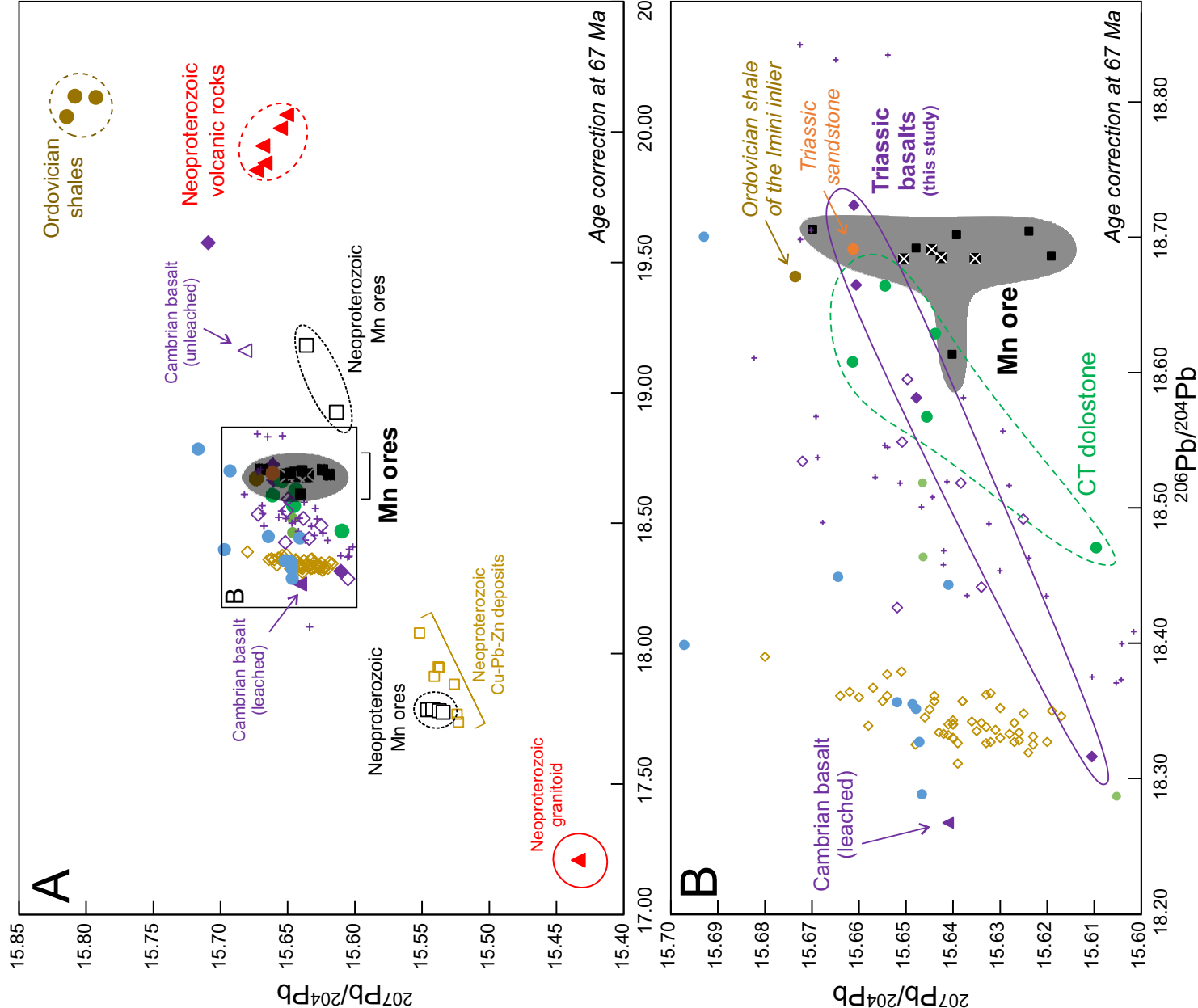
c. 51 Ma



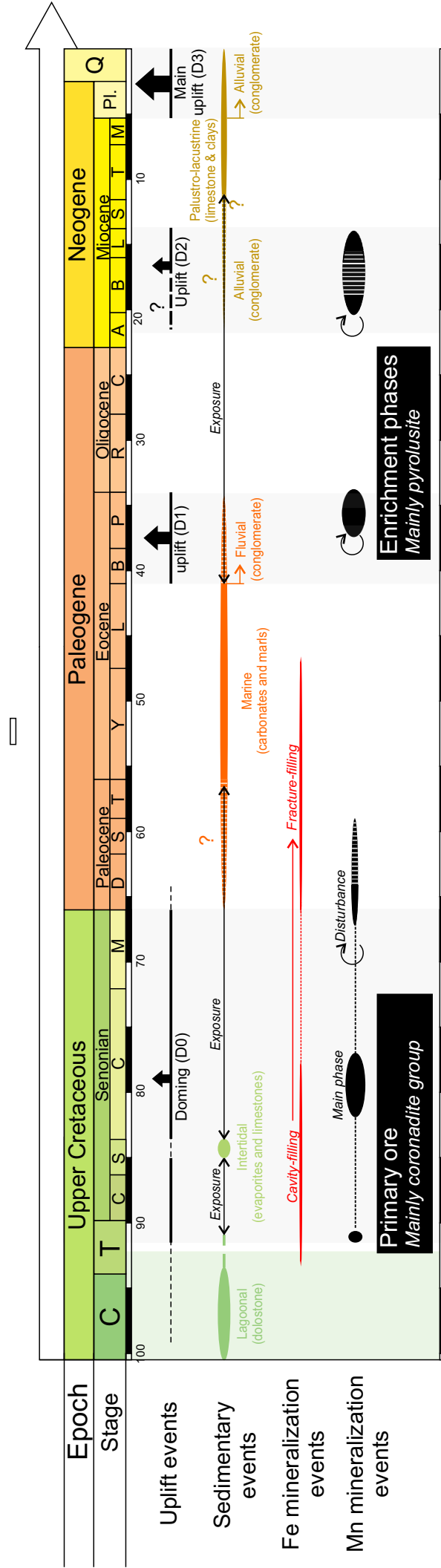
Degassing $(^{39}\text{Ar}/\Delta V_T)/(^{37}\text{Ar}/\Delta V_T)_{\text{me}}$

Degassing $(^{39}\text{Ar}/\Delta V_T)/(^{37}\text{Ar}/\Delta V_T)_{\text{me}}$





- C1-C2 ore
- ⊠ C3 ore
- Mn Neoproterozoic
- ◇ MVT deposits (galena)(Bouadbellah et al. 2012, 2015)
- Neoproterozoic (galena)(Bouadbellah et al. 2016)
- Neoproterozoic (galena)
- Cenomanian-Turonian dolostone
- Jurassic carbonate and sandstone (Bouadbellah et al. 2015)
- Triassic-Senonian gypsum
- Triassic sandstone
- Triassic basalt (leached)
- Triassic basalt (unleached)
- Triassic basalt (Marzoli et al. 2019)
- Ordovician shale
- Cambrian basalt (leached)
- Cambrian basalt (unleached)
- Neoproterozoic felsic rocks

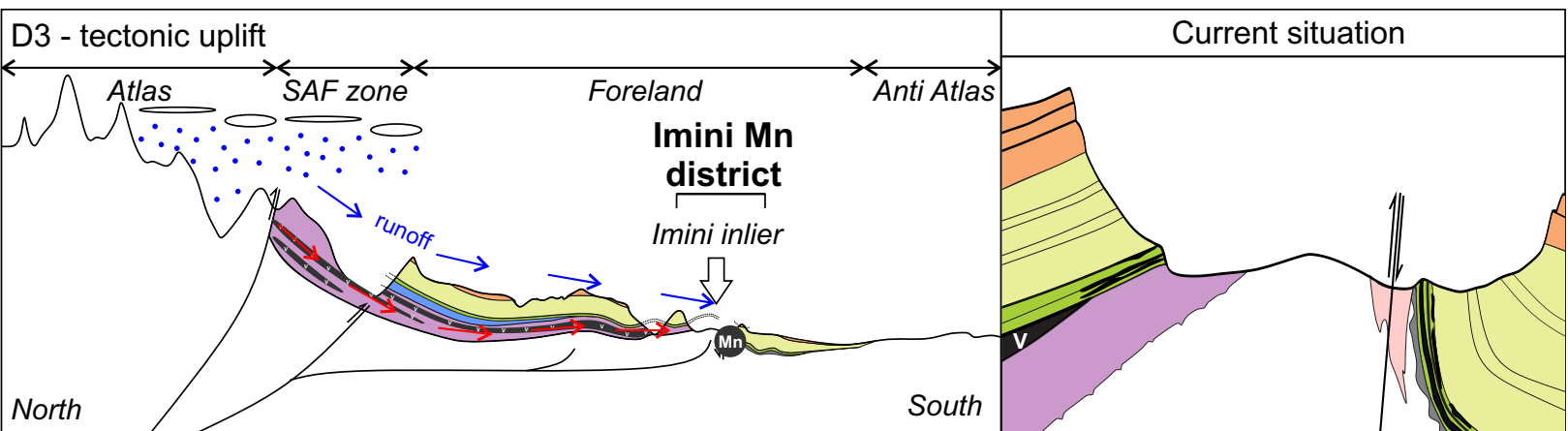
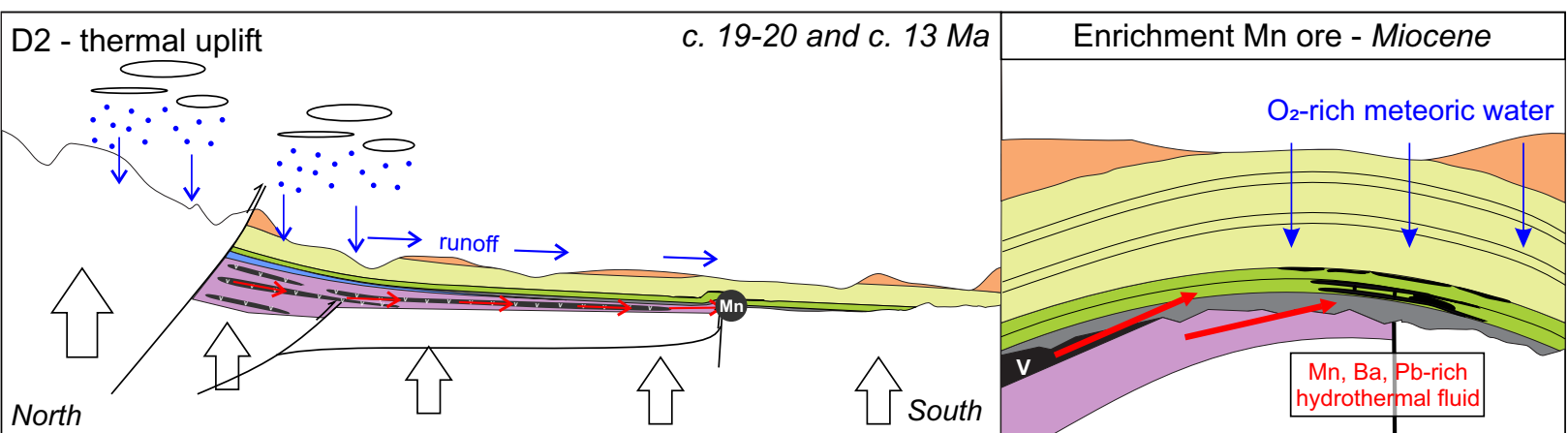
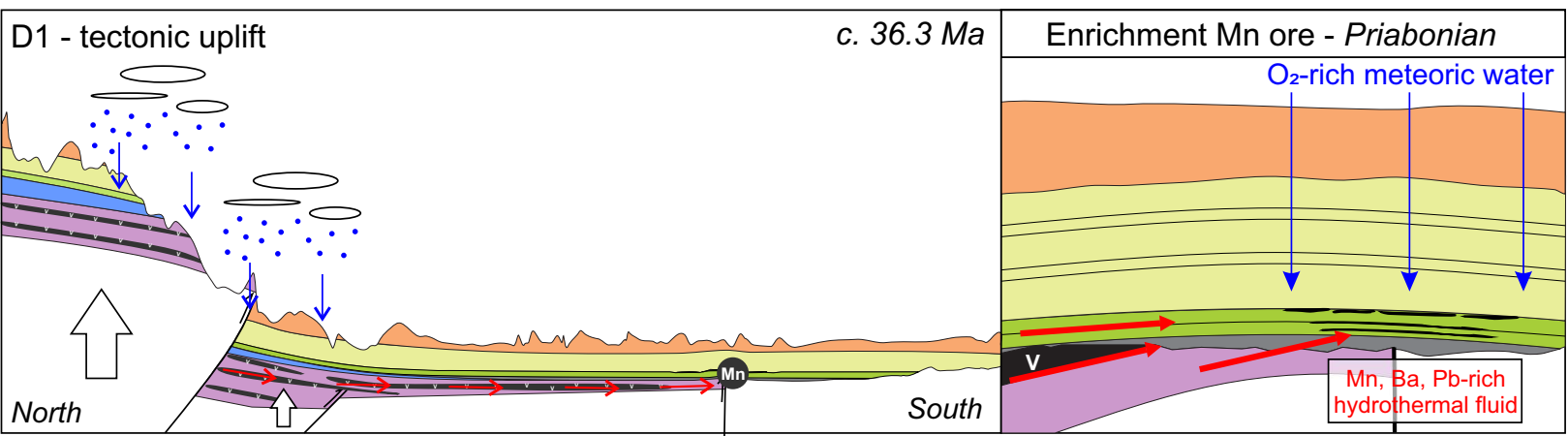
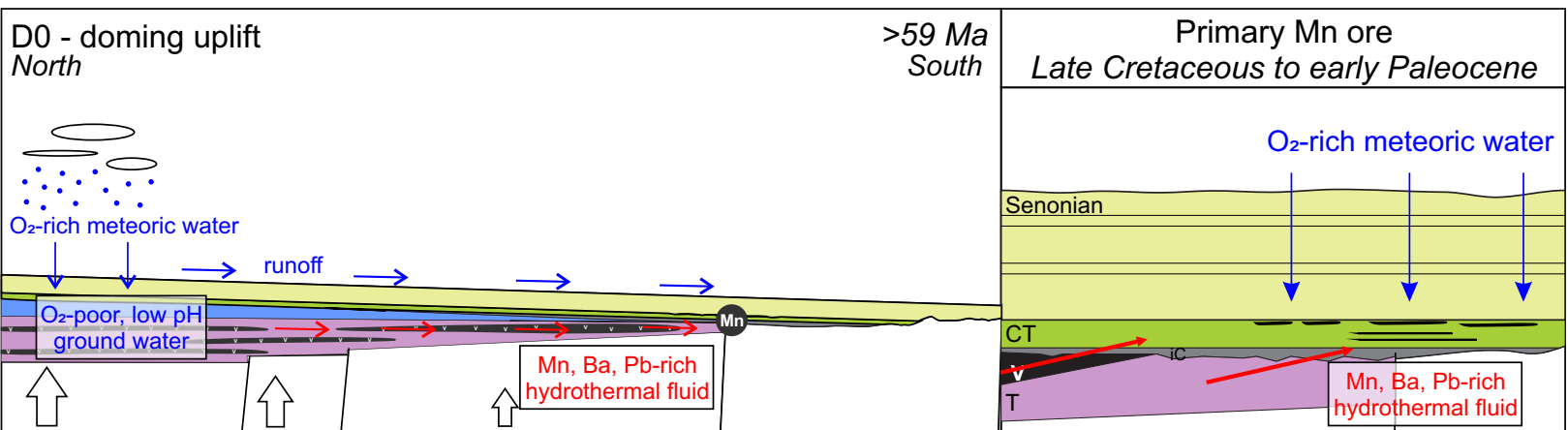


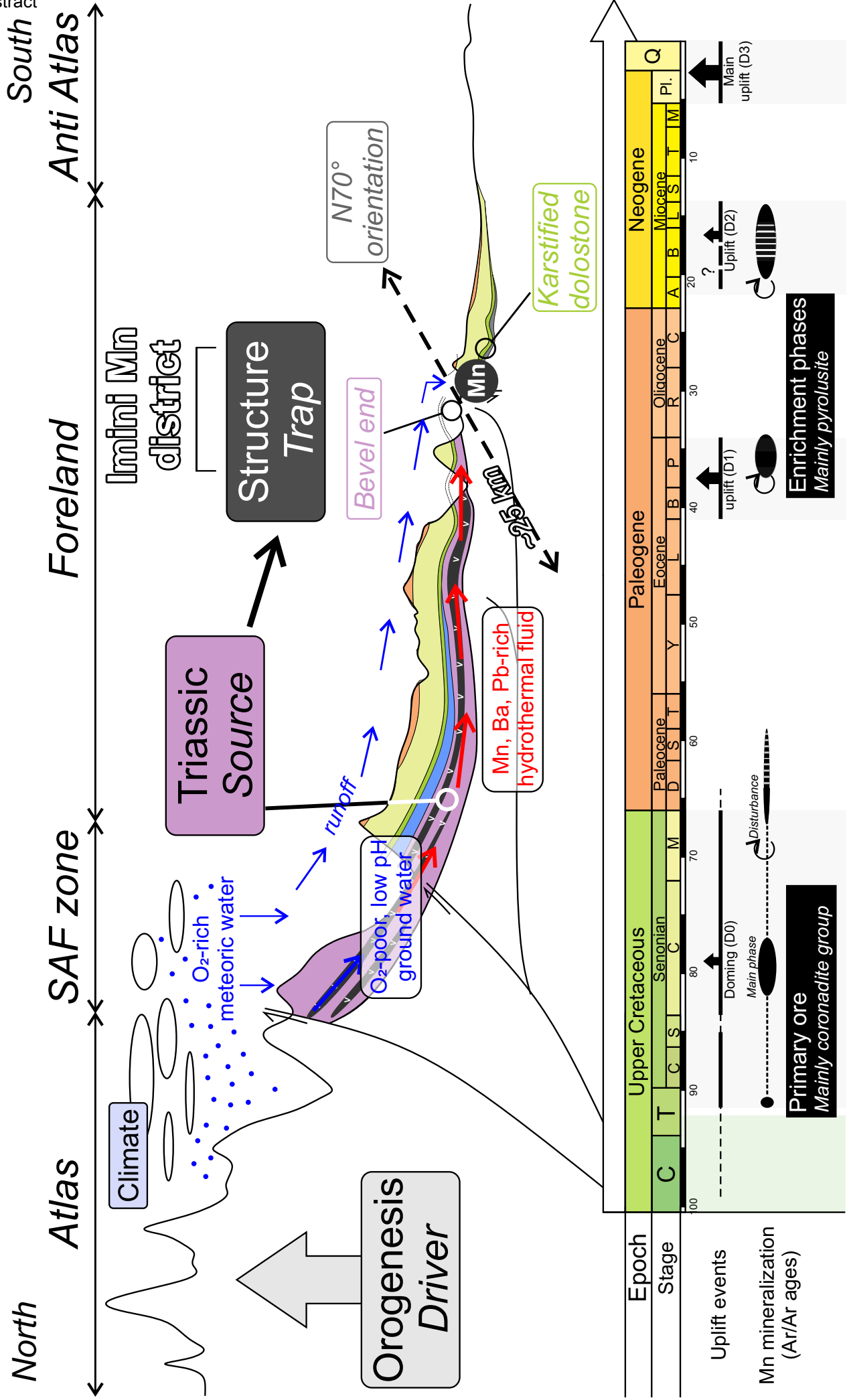
Uplift events

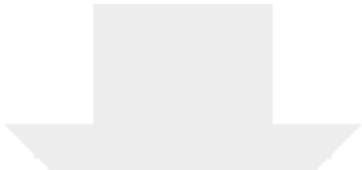
Sedimentary events

Fe mineralization events

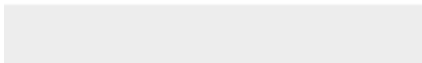
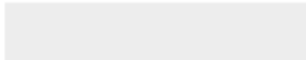
Mn mineralization events

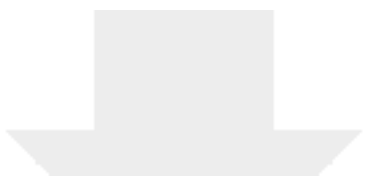






Click here to access/download
Supplementary Material
ESM S1-S6-S7.pdf





Click here to access/download
Supplementary Material
ESMS2-S5.xlsx

